Neuron

Article

Interaction of acetylcholine and oxytocin neuromodulation in the hippocampus

Highlights

- Hippocampal acetylcholine and oxytocin interact in a brain-state-dependent manner
- Acetylcholine and oxytocin distinguish gamma oscillation from sharp-wave ripples
- Acetylcholine suppresses ripples, whereas ripples decrease oxytocin levels
- Acetylcholine modulates oxytocin through a long-loop hippocampal-lateral septum path

Authors

Yiyao Zhang, Mursel Karadas, JingJing Liu, ..., Yulong Li, Richard W. Tsien, György Buzsáki

Correspondence

gyorgy.buzsaki@nyumc.org

In brief

Zhang and Karadas et al. use GRAB sensors and electrophysiology to unravel the interaction of acetylcholine and oxytocin at slow and fast timescales across brain states. Perturbation experiments reveal that acetylcholine modulates oxytocin through the hippocampus-lateral septum path, demonstrating how their cooperative actions enable specific functions.

Zhang et al., 2024, Neuron *112*, 1–14
June 5, 2024
https://doi.org/10.1016/j.neuron.2024.02.021

CellPress

Please cite this article in press as: Zhang et al., Interaction of acetylcholine and oxytocin neuromodulation in the hippocampus, Neuron (2024), https://doi.org/10.1016/j.neuron.2024.02.021

Neuron

CellPress

Article

Interaction of acetylcholine and oxytocin neuromodulation in the hippocampus

Yiyao Zhang,[1,5] Mursel Karadas,[1,5] JingJing Liu,[1] Xinyi Gu,[1] Mihály Vöröslakos,[1] Yulong Li,[4] Richard W. Tsien,[1,2,3] and György Buzsáki[1,2,3,6,*]

[1]Neuroscience Institute, New York, NY, USA
[2]Department of Neurology, Langone Medical Center, New York University, New York, NY 10016, USA
[3]Center for Neural Science, New York University, New York, NY 10003, USA
[4]School of Life Science, Peking University, Beijing, China
[5]These authors contributed equally
[6]Lead contact
*Correspondence: gyorgy.buzsaki@nyumc.org
https://doi.org/10.1016/j.neuron.2024.02.021

SUMMARY

A postulated role of subcortical neuromodulators is to control brain states. Mechanisms by which different neuromodulators compete or cooperate at various temporal scales remain an open question. We investigated the interaction of acetylcholine (ACh) and oxytocin (OXT) at slow and fast timescales during various brain states. Although these neuromodulators fluctuated in parallel during NREM packets, transitions from NREM to REM were characterized by a surge of ACh but a continued decrease of OXT. OXT signaling lagged behind ACh. High ACh was correlated with population synchrony and gamma oscillations during active waking, whereas minimum ACh predicts sharp-wave ripples (SPW-Rs). Optogenetic control of ACh and OXT neurons confirmed the active role of these neuromodulators in the observed correlations. Synchronous hippocampal activity consistently reduced OXT activity, whereas inactivation of the lateral septum-hypothalamus path attenuated this effect. Our findings demonstrate how cooperative actions of these neuromodulators allow target circuits to perform specific functions.

INTRODUCTION

Neuronal traffic in the brain, in addition to fast spike transmission communication, is strongly regulated by a handful of subcortical neuromodulators affecting neurons by activation of mainly metabotropic receptors, each with different properties and innervation patterns, and therefore exerting unique impacts on the computational function of neuronal circuits. Identifying the role of neuromodulators at the fine timescale dynamics of circuit function has become possible only recently by the emergence of novel techniques enabling the monitoring of their release and receptor binding kinetics.[1,2]

Acetylcholine (ACh) is among the most extensively investigated neuromodulators with a variety of brain targets and receptor-dependent unique properties.[3,4] ACh is thought to be critical for hippocampus-dependent episodic memories,[5,6] working memory[5,7] and it may bring about its beneficial cognitive effects by enhancing theta rhythm oscillations, theta-gamma coupling, affecting hippocampal sharp-wave ripples (SPW-Rs), decreasing recurrent excitation, and increasing synaptic plasticity.[6,8–11] Cholinomimetic drugs can enhance episodic memory and are used for the treatment of Alzheimer's disease.[12] Social memory is a particular form of episodic memory since social events are also embedded in space and time. Social memories also depend on the hippocampus but are assumed to involve the neuromodulator oxytocin (OXT), produced in the paraventricular and supra-optic nuclei of the hypothalamus.[13–17] Impairment of tonic OXT signaling is thought to underlie cognitive and emotional dysfunction associated with autism spectrum disorders, schizophrenia, and aging.[18–20] In addition to social interactions, OXT may also contribute to non-social operations of the brain, such as brain "state" regulations,[21] in cooperation with other neuromodulators.

In general, understanding the role of neuromodulators at the timescale of brain circuit operations requires both monitoring their interactions and correlations with physiologically identified network patterns. In turn, these correlations should be contrasted with perturbation of neuromodulator activity to gain more direct insights into causal effects.[6] We addressed these broad problems by simultaneous fiber-photometric measurements of ACh and OXT variations in the hippocampus, using G-protein-coupled receptor activation-based ACh ($GRAB_{ACh}3.0$ and $GRAB_{rACh}1.4$) and OXT ($GRAB_{OXT}1.7$) sensors.[22,23] These optical measurements were compared with sleep-wake changes and characteristic brain-state-dependent fine timescale changes of neuronal activity, including theta, gamma oscillations, SPW-Rs, sleep spindles, and population spike synchrony. In turn, we tested the direction of neuromodulation-network pattern

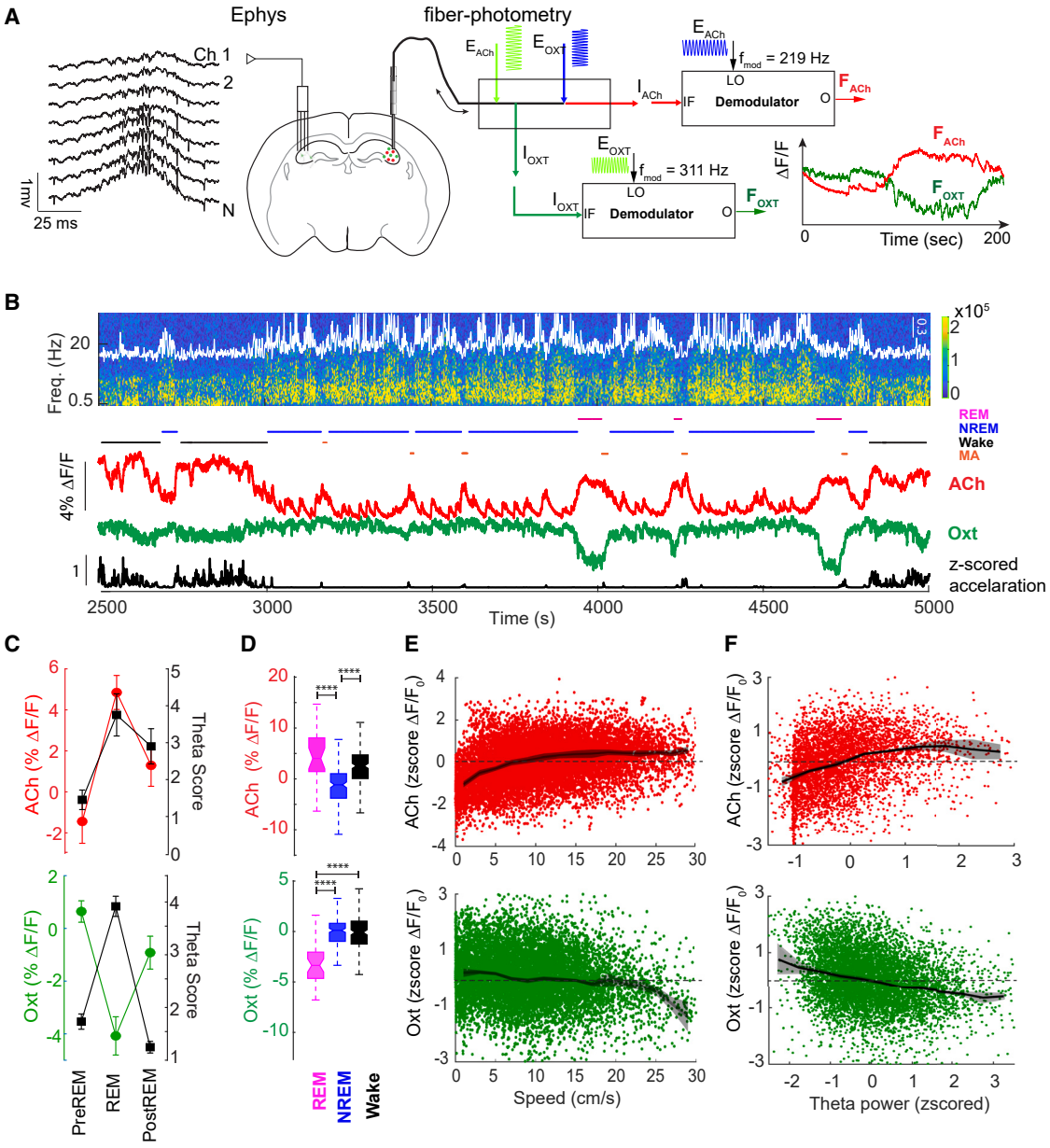

Figure 1. Global brain state correlates of ACh and OXT

(A) Experimental design. Hippocampal electrophysiological signal (LFP and spikes) recorded by a silicon probe. Dual-color fiber-photometry setup using lock-in detection technique. E, excitation; I, intensity of emission; LO, local oscillator; and F, fluorescence.

(B) Example traces of simultaneously recorded ACh and OXT fluorescence ($\Delta F/F_0$), acceleration signal of the mouse's head, time-resolved spectrogram, and brain-state scoring. The white line superimposed on the spectrogram is the integrated power of sleep spindles (10–20 Hz band; *Z* scored). Note strikingly opposite ACh and OXT signals during REM and waking movement.

(C) Group results for ACh ($\Delta F/F_0$: mean ± SEM, one-way ANOVA, p = 0.0003. Holm-Šídák's multiple comparisons test: preREM vs. REM, p < 0.0001, preREM vs. postREM, p = 0.0204, REM vs. postREM, p = 0.0081. n = 26 REM packets in 7 mice), OXT ($\Delta F/F_0$: mean ± SEM, one-way ANOVA, p < 0.0001. Holm-Šídák's multiple comparisons test: preREM vs. REM, p < 0.0001, preREM vs. postREM, p = 0.0172, REM vs. postREM, p < 0.0001. n = 41 REM packets in 5 mice) and theta score (the ratio of relative spectral power in the 5–10 and 0.5–4 Hz bands: ACh, mean ± SEM, one-way ANOVA, p < 0.0001. Holm-Šídák's multiple comparisons test: preREM vs. REM, p = 0.0002, preREM vs. postREM, p = 0.0182, REM vs. postREM, p = 0.1170. n = 26 REM packets in 7 mice; OXT, mean ± SEM, one-way ANOVA, p < 0.0001. Holm-Šídák's multiple comparisons test: preREM vs. REM, p < 0.0001, preREM vs. postREM, p = 0.0039, REM vs. postREM, p < 0.0001. n = 41 REM packets in 5 mice) during REM and during equal length preceding and following NREM epochs.

(legend continued on next page)

Please cite this article in press as: Zhang et al., Interaction of acetylcholine and oxytocin neuromodulation in the hippocampus, Neuron (2024), https://doi.org/10.1016/j.neuron.2024.02.021

relationships by optogenetic control of ACh and OXT neurons. Our findings offer a comprehensive description of how the cooperative actions of these neuromodulators could enable hippocampal circuits to perform specific network functions. We also uncover a long-loop mechanism by which synchronous population activity of hippocampal neurons acts through a hippocampus-lateral septum (LS) -hypothalamus path to regulate oxytocinergic neuronal activity.

RESULTS

We first describe the correlations between ACh and OXT and the known slow- and fast-changing network patterns in the hippocampus. Next, we challenge the observed correlations by optogenetic perturbations. Finally, we examine the circuit mechanism of interaction between ACh and OXT.

Spontaneous oscillations of hippocampal ACh and OXT levels

To monitor the dynamics of extracellular ACh and OXT, we simultaneously (n = 4 mice) or separately (ACh: n = 5 mice, OXT: n = 5 mice) imaged the activities of muscarinic receptor-based green fluorescence indicator $GRAB_{ACh3.0}$ and red fluorescence indicator $GRAB_{rACh1.4}$, and OXT receptor-based green fluorescence indicator $GRAB_{OXT1.7}$ (an improved version of $GRAB_{OXT1.0}$[23]), from the hippocampus of freely moving mice in their home cage. In the simultaneous recording experiments, adeno-associated virus (AAV) with human-synapsin (hSyn) promoter encoding indicator $GRAB_{rACh1.4}$ and $GRAB_{OXT1.7}$ were injected together into one hemisphere of the dorsal hippocampus (Figure 1A), whereas in separate experiments, ACh3.0 or OXT1.7 was injected into the dorsal hippocampus of separate animals. 3 weeks after virus injection, an optic fiber (400 μm) was implanted above the CA1-2 pyramidal cell layer (Figures 1A and S1A). In the same surgery, a multi-shank silicon probe was also implanted into the other hemisphere to record the local field potential (LFP) and extracellular action potentials (spikes) of neurons (Figures 1A and S1B). Brain states (wake state [WAKE], rapid eye movement [REM], and non-REM [NREM]) were classified with a combination of LFP, electromyography (EMG), and movement or acceleration (Figure 1B).[24] NREM was characterized by increased power of slow oscillations, coupled to sleep spindles (Steriade et al.[25]), and quasi-periodic oscillations at approximately 0.02–0.05 Hz of both ACh and OXT (Figures 2B, 2D, and 2E). ACh and OXT signals were generally anti-correlated ($r = -0.26 \pm 0.07$, $p = 0$, n = 6 session/3 mice with dual-color simultaneous recording), as well as during NREM-WAKE and NREM-REM transitions, with ACh reaching peak values during REM sleep when OXT had its minimum (Figures 1B–1D, S3, and S4). Both locomotion speed and theta power showed a positive correlation with ACh fluorescence (Figures 1E and 1F), with the steepest increase between immobility and movement initiation (~2 cm/s). By contrast, the OXT signal negatively correlated with both speed and theta power (Figures 1E and 1F).

To examine the relationship between electrophysiological and neuromodulator patterns within and across brain states, we calculated the correlation between ACh and OXT fluorescence fluctuations on the one hand and delta band (0.5–4 Hz) power, sleep spindle power (sigma band power, 10–20 Hz), and gamma band power (30–100 Hz; Figures 2, 3, and S4) (Sullivan et al.[26]) on the other. In addition, we correlated ACh and OXT signal fluctuations. NREM episodes were divided into "packets" (i.e., intervals between microarousals) based on the spectral power of the LFP and accelerometer recordings, and the packet durations were normalized.[22] The power of the delta band and sleep spindle band (sigma) increased monotonically within packets of NREM, parallel with the continuous decrease of ACh and OXT signals (Figures 2A and 2B). The ends of the packets were marked by microarousals (i.e., increased muscle activity or acceleration) and decreased delta and sigma power.[24] This state change was associated with a rapid increase in ACh fluorescence, with an ensuing delay in the increase of OXT signal (Figures 2C and S4E). In the frequency domain, spectral analysis revealed a prominent coherence peak in the 0.02–0.05 Hz band (packet duration; or ultraslow oscillation; Figure 2A) between both neuromodulators and the power of sleep spindles (sigma power) as well as between ACh and OXT signals (Figure 2D). In the time domain, cross-correlation of the signals showed an inverse correlation between sigma power and both neuromodulators during NREM and a positive correlation between ACh and OXT signals (Figure 2E). This analysis also showed an approximately 2 s lead of the ACh fluorescence before OXT (Figure 2E). Thus, spontaneous fluctuation of ACh and OXT levels were largely anti-correlated across behavioral states at slower timescales, whereas a time-shifted relationship was visible at finer timescales.

Neuromodulator levels separate gamma oscillations and SPW-Rs

Brain-state changes are associated with characteristic oscillations in unique frequency bands (Buzsaki and Draguhn[27]). Gamma band power (30 to >100 Hz, especially "high gamma bursts," 50–400 Hz,[28,29] tends to be highest during active waking, associated with theta oscillations.[30,31] By contrast, SPW-Rs are present only when theta oscillations are absent.[32–38] Because of the overlapping frequencies and similar durations of fast-gamma bursts and ripples, their physiological distinctness is hotly debated.[32–34,36,37,39–41] To relate these oscillatory patterns to brain-state-dependent neuromodulator tone, we constructed time-resolved power spectra centered

(D) ACh and OXT fluorescent signals during REM (42 episodes of OXT, 26 episodes of ACh), NREM (195 episodes of OXT, 184 episodes of ACh), and WAKE (200 episodes of OXT, 211 episodes of ACh). One-way ANOVA, $p < 0.0001$ in OXT and ACh groups. Holm-Šídák's multiple comparisons test: ACh, WAKE vs. REM, $p = 0.0726$, REM vs. NREM, $p < 0.0001$, NREM vs. WAKE, $p < 0.0001$; OXT, WAKE vs. REM, $p < 0.0001$, REM vs. NREM, $p < 0.0001$, NREM vs. WAKE, $p = 0.2559$.
(E) Relationship between locomotion speed and ACh, OXT signals (n = 6 sessions/3 mice, r: 0.41 ± 0.09, $p < 0.0001$, and n = 5 sessions/3 mice, respectively, r: -0.15 ± 0.07, $p < 0.0001$). Note rapid changes in the low-speed range for ACh. Lines, running averages ± SEM.
(F) Relationship between theta power and ACh, OXT signals (n = 3 sessions/3 mice for both. ACh-theta power r: 0.32 ± 0.03, $p < 0.0001$. OXT-theta power r: -0.24 ± 0.05, $p < 0.0001$.). Normalized theta power <0 corresponds to immobility epochs.

Please cite this article in press as: Zhang et al., Interaction of acetylcholine and oxytocin neuromodulation in the hippocampus, Neuron (2024), https://doi.org/10.1016/j.neuron.2024.02.021

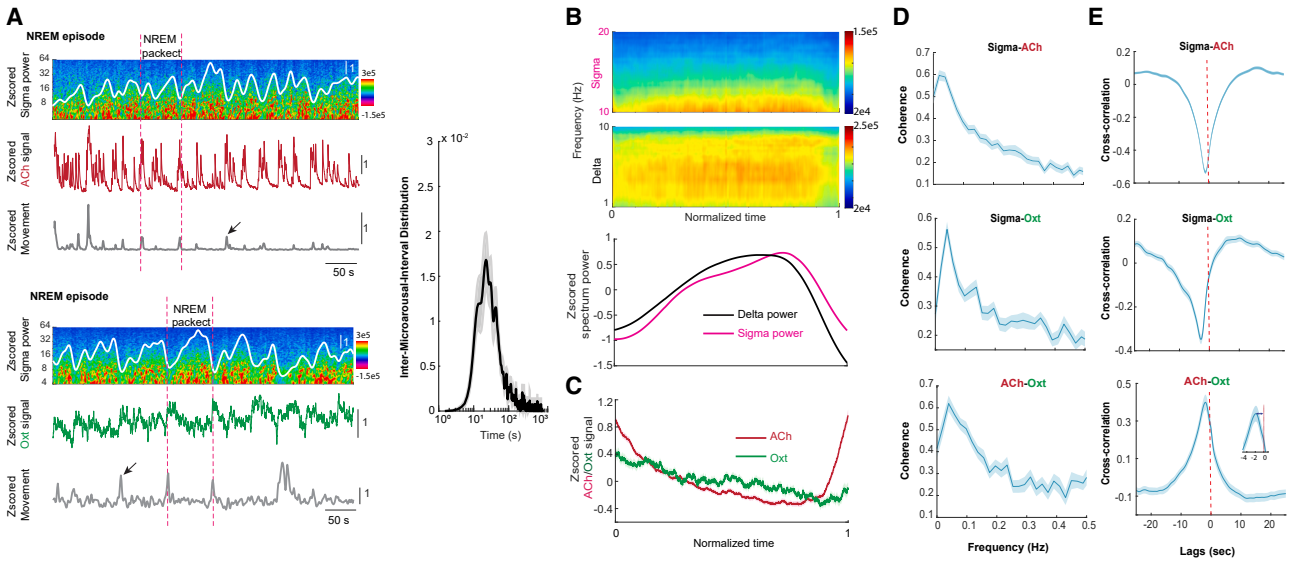

Figure 2. ACh and OXT dynamics during NREM packets

(A) Covariation of spectrogram with superimposed sleep spindle power (sigma; white line, *Z* scored), ACh or OXT fluorescence (top and bottom, respectively), and movement. Vertical dashed lines indicate NREM packets, defined as epochs between the troughs of spindle power and microarousals (black arrows). Right, log-distribution of packet intervals. y axis, probability of occurrence. Mean ± SEM, n = 780 NREM packets in 8 mice. Note peak between 10 and 100 s.

(B) Spectrogram for time-normalized NREM packets (mean ± SEM, n = 780 NREM packets in 8 mice). Lower, time-normalized delta, and sigma power.

(C) ACh (mean ± SEM, n = 520 NREM packets/4 mice, bottom red) and OXT signals (mean ± SEM, n = 260 NREM packets/4 mice, bottom green), n = 780 NREM packets in 8 mice.

(D) Spectral coherence between spindle power and ACh (top, n = 90 episodes/4 mice, mean ± SEM), spindle power and OXT (middle, n = 64 episodes/4 mice, mean ± SEM), and ACh and OXT (bottom, n = 46 episodes/2 mice with simultaneous dual-color recordings, mean ± SEM). Note peak coherence at ~0.02–0.04 Hz.

(E) Cross-correlograms between the three different signals. Note that ACh leads OXT signal by about 2 s (inset).

on peaks and troughs of ACh and OXT signals, respectively, during NREM and active waking (WAKE; Figures 3A–3D).

For quantitative comparison, we used hippocampal LFP recorded in CA1 the str. radiatum for gamma (where gamma power is largest[42]) and the pyramidal layer for ripple power detection (since ripple power is largest[43]) during active waking (locomotion) and NREM sleep, respectively. During NREM, ripple power reached its minima and maxima when levels of ACh were highest and lowest, respectively (Figures 3A, 3E, and 3F). Surges of ACh were associated with decreased wide-band power, including the broad gamma band. By contrast, during WAKE, gamma power positively correlated with the ACh signal (Figures 3B, 3G, and 3H). Troughs and peaks of the OXT signal were preceded by a surge or dip of ripple power, respectively (Figures 3C and 3E). During WAKE and REM, the increase and decrease of gamma-band power preceded the troughs and peaks of OXT signal, which is opposite to gamma-ACh correlations (Figures 3D, 3G, and S6). These findings demonstrate brain-state-dependence of neuromodulator effects. Further, knowledge about neuromodulator tone can reliably distinguish between gamma and ripple oscillations.

To disambiguate the potential uncertainty in detecting the peaks and troughs of the fluorescent signals, we performed a complementary analysis in the reverse direction. We sampled ACh and OXT fluorescence centered on the occurrence of isolated SPW-Rs (≤1 event per second), SPW-R doublets (2 event/s), and SPW-R clusters (≥3 events/s) during NREM (Figure 4A). The maximum probability of SPW-Rs in each group coincided with the trough of a slow decrease-increase of the ACh signal (Figure 4A). The OXT signal reached a minimum of ~2 s after the SPW-R after which the signal slowly recovered parallel with that of ACh (Figures 4A and 4B). This tri-partite temporal relationship between ACh and OXT fluorescence and SPW-Rs remained similar whether ACh and OXT were imaged separately in different experiments or simultaneously in the same animal (Figure 4B). The fastest rate change of the fluorescent signal was observed for OXT after the SPW-R (e.g., Figures 4B and S5), demonstrating that the slower kinetics of the OXT sensor, compared with that of the ACh sensor, is not the cause of the observed ~2 s ACh-OXT time offset.

These results raised the possibility that the sharp decrease of OXT is brought about by the synchronous neuronal activity underlying SPW-Rs. To test this hypothesized role of hippocampal synchrony, we examined the effect of population synchrony outside SPW-R. We separated four levels of synchrony magnitudes from the broad distribution of multiple unit activity (MUA; Figure 4C) and sampled the fluorescent signals of the neuromodulators centered around the synchronous events, analogous to the SPW-R sampling. During NREM, we detected a fast decrease of OXT fluorescence, reaching a minimum ~2 s after the MUA synchrony (Figure 4E). As expected, MUA synchrony vs. ACh and OXT signals showed a similar relationship to SPW-Rs during NREM (Figures 4D and 4E;

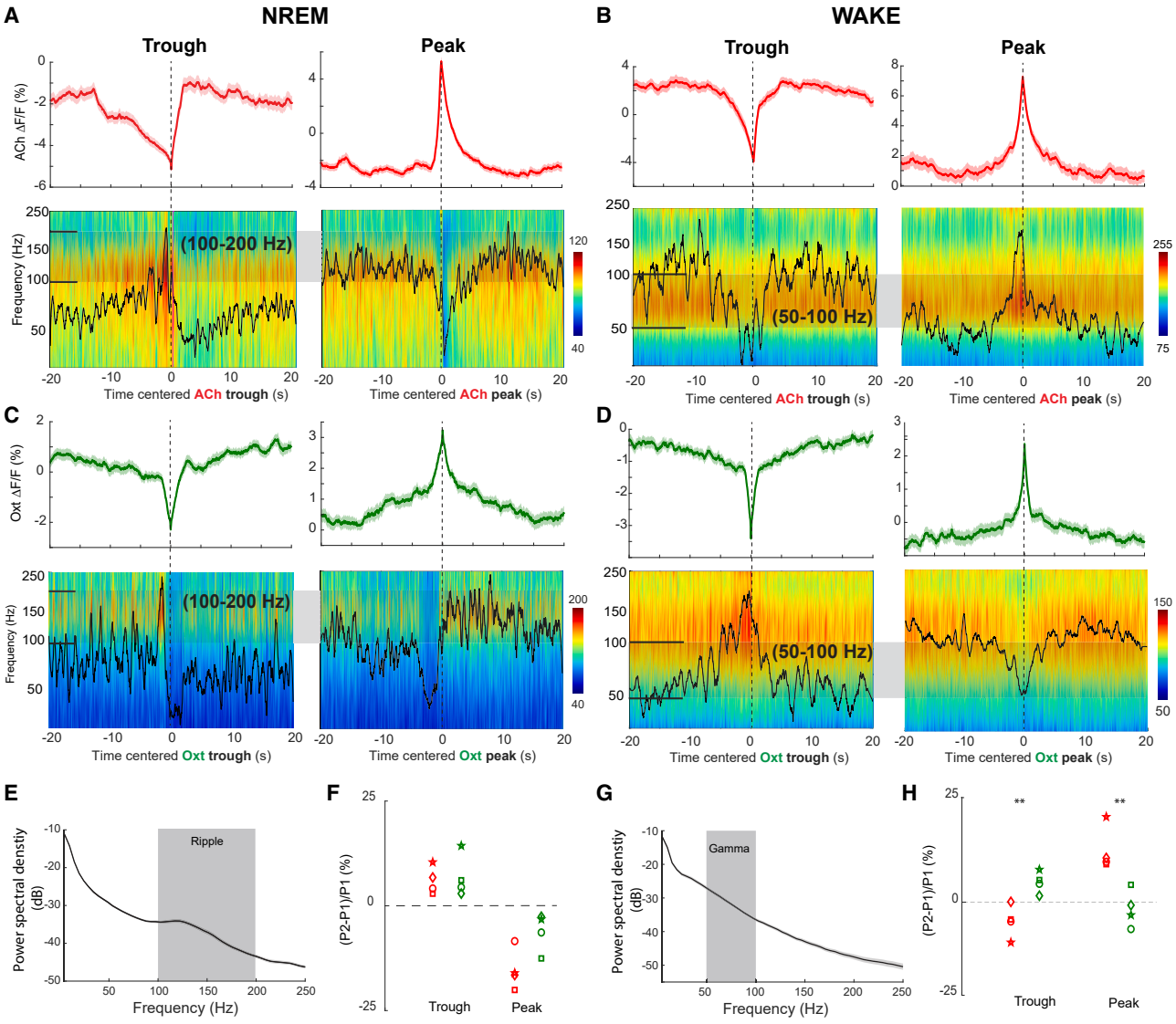

Figure 3. State-dependent correlations of gamma and ripple band activity vs. ACh and OXT

(A and C) NREM; (B and D) waking. Mean ± SEM trace.

(A) Averaged traces of ACh signal (top, red trace), and spectrogram of LFP from the CA1 pyramidal layer, centered on trough (left) or peak (right) of ACh signal. Power is color-coded, and the range is different in (A)–(D) to highlight changes in gamma and ripple bands. Black line, average power in the ripple band (measured between 100–200 Hz; horizontal lines on spectrogram; *Z* scored).

(B) Same display as in (A), but during active waking (>2 cm/s speed epochs) and from recordings in CA1 stratum radiatum. Black line indicates integrated gamma power in the 50–100 Hz band.

(C and D) Same as (A) and (B) but for OXT (green trace). Each panel is a single session.

(E) Power spectrum of CA1 LFP during NREM. Shaded area indicates ripple band.

(F) Group results of ACh (n = 4 sessions in 3 mice) and OXT (n = 4 sessions in 4 mice). P1: power between −20 and −15 s, P2: power between −3 and 2 s. Ripple power difference at ACh and OXT troughs: p = 0.78, difference at ACh and OXT peaks: p = 0.03 unpaired t test with two-sample equal variance.

(G and H) Same as (E) and (F) but during waking. Shaded area indicated the integrated gamma band, recorded from CA1 str. radiatum. Troughs: **p = 0.008, peaks: p = 0.006 unpaired t test with two-sample equal variance.

statistical results are shown in Table S1). By contrast, during waking, the magnitude of MUA synchrony increased with ACh (Figure 4D), as was the case for gamma power (Figure 3B). The OXT signal decreased immediately after the MUA surge, similar to NREM, although to a smaller extent (Figure 4E). These observations suggest that the relationship between ACh hippocampal synchrony is brain-state-dependent. During NREM, population synchrony and ACh levels are anti-correlated, whereas in the waking animal, ACh may promote MUA synchrony and gamma oscillations. By contrast, OXT level is consistently reduced following synchronous activity of the hippocampal output.

Please cite this article in press as: Zhang et al., Interaction of acetylcholine and oxytocin neuromodulation in the hippocampus, Neuron (2024), https://doi.org/10.1016/j.neuron.2024.02.021

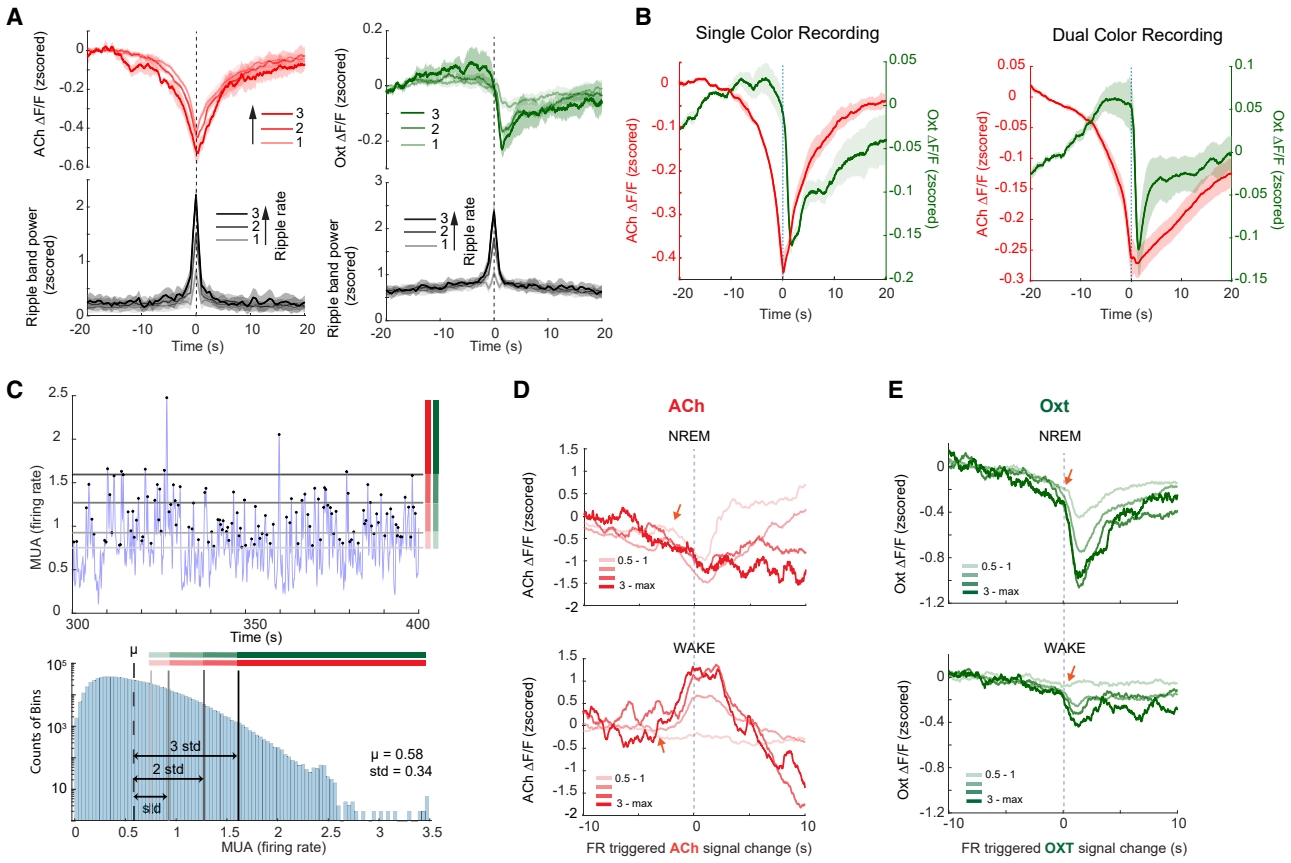

Figure 4. Temporal relationships between SPW-R, population spike bursts, ACh, and OXT

(A) Temporal correlation between SPW-Rs and ACh (left) and OXT (right), mean ± SEM trace. Time 0, occurrence of SPW-Rs in 3 groups: 1, 2, 3, or more SPW-Rs/s. Note that SPW-R bursts are correlated with larger decreases of ACh (n = 6 sessions/5 mice) and OXT (n = 4 sessions/4 mice).

(B) Overlayed averaged ACh and OXT traces (mean ± SEM) for all experiments, centered on SPW-Rs (0 s; left panel). Note the maximum probability of SPW-Rs occurrence at the minimum of ACh and ~2 s delay of the OXT trough (arrow) after SPW-R (same mice as in A). Right, same as the left, but ACh and OXT were measured simultaneously from the same optic fiber (n = 5 sessions/3 mice). Green arrows indicate the trough of OXT signal after the SPW-R. The vertical color bar shading indicates MUA groups separated into 4 magnitude classes (used for comparison with ACh and OXT signal in D and E, respectively).

(C) Illustration of quantification of the magnitude of synchrony (multiple unit activity in 10 ms windows). The horizontal lines indicate the 4 quartiles of the synchronous events. SPW-Rs were excluded from these synchronous events.

(D and E) (D) ACh signal, centered on peak of MUA synchrony level (0 s) during NREM and active waking. Color shades refer to the quartile magnitudes in (C). Note opposite changes related to synchronous events in the two brain states. (n = 5 sessions/3 mice, mean ± SEM trace) (E). Same as (D) for OXT. Note MUA synchrony-correlated decrease of OXT ~2 s after the hippocampal population spike event (arrow; n = 4 sessions/4 mice, mean ± SEM trace, NREM: $p < 0.0001$, one-way ANOVA. WAKE: $p < 0.0001$, one-way ANOVA. Post-hoc Holm-Šídák's multiple comparisons test). Red arrows in (D) and (E) point to approximate times of fast signal changes.

Optogenetic manipulation of ACh and OXT affects SPW-R occurrence

To challenge the observed correlations with perturbation experiments, we virally expressed the inhibitory halorhodopsin (eNpHR3.0) or excitatory channelrhodopsin (ChR2) in the medial septum (MS) of ChAT-Cre mice and ChR2 in the hypothalamic paraventricular nucleus (PVN)[44] of OXT-Cre mice (Figure 5). Optogenetic silencing of MS cholinergic neurons during NREM (n = 4 mice) increased the power in the sleep spindle and ripple bands, firing rates of both pyramidal cells and putative interneurons as well as the probability of SPW-R (Figure 5A). In a complementary fashion, optogenetic activation of MS cholinergic neurons (n = 4 mice) decreased spindle and ripple band activity and virtually abolishing SPW-Rs (Figure 5B), confirming previous results.[6,10] MS activation during NREM increased and decreased the firing rates of interneurons and pyramidal cells, respectively (Figure 5B). Optogenetic activation of OXT neurons in PVN also decreased ripple power and SPW-R occurrence, but it had less pronounced effects on neuronal firing compared with cholinergic activation (Figure 5C). Thus, although ACh and OXT exerted qualitatively similar effects on SPW-Rs and firing patterns of single neurons during NREM, the two neuromodulators showed an opposite relationship during active waking and REM, suggesting a complex physiological relationship between these two neuromodulators.

The temporal lead of ACh over OXT suggests that cholinergic activity may regulate OXT signaling. OXTergic neurons can be affected directly by ACh release from cholinergic neurons in

Please cite this article in press as: Zhang et al., Interaction of acetylcholine and oxytocin neuromodulation in the hippocampus, Neuron (2024), https://doi.org/10.1016/j.neuron.2024.02.021

CellPress

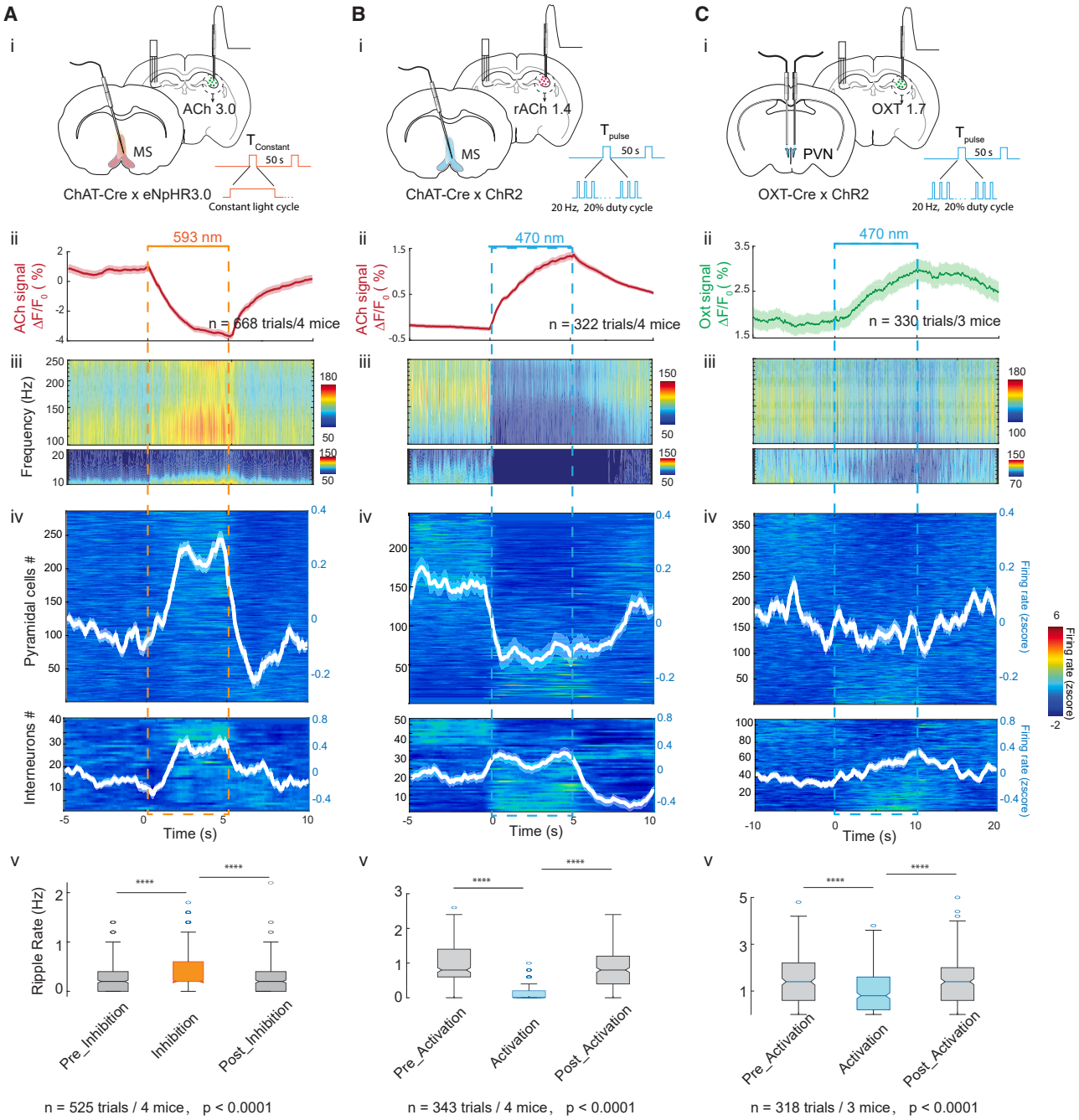

Figure 5. Effect of optogenetic manipulation of ACh and OXT on hippocampal firing rates and SPW-Rs

(A) (i) Schematics of the experiments. (ii) ACh signal change in response to 5 s light pulse activation of inhibitory halorhodopsin (eNpHR3.0)-infected medial septum (MS) cholinergic neurons (mean ± SEM trace), (iii) corresponding average spectrogram of CA1 str. pyramidale LFP (power change is color-coded), and (iv) rate-normalized firing of pyramidal cells and interneurons. Each line corresponds to a single neuron. Relative change is color-coded (right color bar). White curves superimposed on the spike raster plots correspond to population means (y axis is on the right, *Z* scored). (v) SPW-R occurrence before, during, and after suppression of cholinergic neurons. N = 4 mice, **** $p < 0.0001$, paired t test.

(B) Same as (A), but during optogenetic activation of ChR2-expressing MS cholinergic neurons (n = 4 mice).

(C) Same arrangement as in (A), but during optogenetic activation of ChR2-expressing OXT neurons in the paraventricular nucleus (PVN) of hypothalamus (n = 3 mice). Note increased rate of SPW-Rs during cholinergic suppression and their suppression during both cholinergic and OXT activation. All traces in (A)–(C) are mean ± SEM trace.

Please cite this article in press as: Zhang et al., Interaction of acetylcholine and oxytocin neuromodulation in the hippocampus, Neuron (2024), https://doi.org/10.1016/j.neuron.2024.02.021

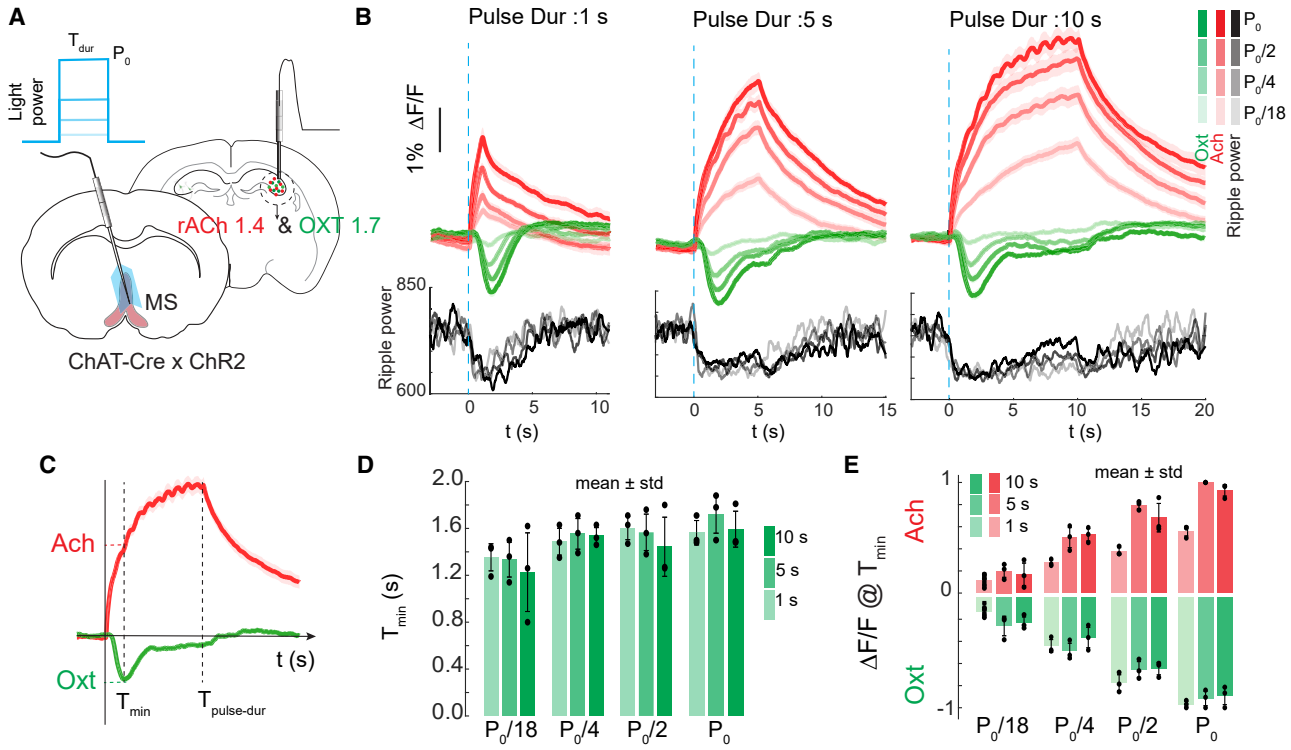

Figure 6. Cholinergic activation-induced suppression of OXT

(A) Schema of optogenetic activation of MS cholinergic neurons and simultaneous measurements of hippocampal ACh and OXT.

(B) Example session of change of OXT fluorescence in response to 3 durations of 4 different power levels of stimulation, mean ± SEM trace. Bottom panel, spectrum power in ripple band (arbitrary units). P_0 is the maximum intensity in each experiment ($P_0/2$ is half the maximum, etc.). (Pulse Duration: (1 s): ACh, ***p = 0.0005; OXT, **p = 0.0057. Pulse Dur (5 s): ACh, **p = 0.0065; OXT, *p = 0.0179. Pulse Dur (10 s): ACh, **p = 0.0092; OXT, *p = 0.0101. Repeated measures one-way ANOVA, n = 3 mice. *Pulse Amplitude* ($P_0/18$): ACh, **p = 0.0096; OXT, **p = 0.0072. Pulse amp ($P_0/4$): ACh, **p = 0.0019; OXT, ***p = 0.0002. Pulse amp ($P_0/2$): ACh, **p = 0.0064; OXT, *p = 0.0127. Pulse amp (P_0): ACh, **p = 0.0026; OXT, **p = 0.0019. Post-hoc multi-comparison statistical results are in Tables S2 and S3).

(C) Averages across all 10 s stimuli. Note the fast (phasic) drop and tonic depression of OXT signal.

(D) Latency of OXT minima.

(E) ACh and OXT magnitude values at OXT minima (T_{min}) at various stimulus intensities and durations (n = 4 sessions/4 mice).

the hypothalamus,[45,46] brainstem, and basal forebrain[47] or indirectly via a hippocampus-LS-hypothalamus path.[48,49] We tested these possibilities by optogenetic stimulation of MS cholinergic neurons during NREM (Figure 6A). As expected, optogenetic activation of cholinergic neurons increased ACh fluorescence in the hippocampus in a light-intensity and duration-dependent manner (Figures 6B and 6C). Statistical results are shown in Tables S2 and S3). At the same time, the stimulation induced a rapid drop of the OXT signal, which consisted of a phasic and tonic component. The phasic component had a minimum 1.44–1.79 s after the stimulation onset (Figure 6D), reminiscent of the ~2 s delay between ACh and OXT after SPW-Rs and synchronous bursts of CA1 neurons. We quantified the impact of cholinergic activation on OXT by measuring the magnitude of the OXT signal at the trough of the phasic response. The dip of OXT showed a largely linear correlation with the magnitude of OXT signaling (Figure 6E), followed by a sustained tonic component of OXT fluorescence throughout the stimulus duration (Figure 6A).

The optogenetic experiments also offered the opportunity to quantify the *in vivo* kinetics of ACh and OXT. Compared with ACh (response time constant, $\tau_{ACh3.0} = 1.55$; $\tau_{rACh1.4} = 2.48$; recovery, $\tau_{ACh3.0} = 1.51$; $\tau_{rACh1.4} = 4.09$;), both the response time constant and recovery time constant of OXT were several-fold slower (response time constant, $\tau_{OXT1.7} = 14.53$; recovery, $\tau_{OXT1.7} = 17.97$).

The optogenetic manipulations supported the hypothesis that ACh exerts control on OXT. To identify the potential circuit-induced effect of cholinergic activity on OXT neurons via the hypothesized hippocampus-LS path (Figure 7C), we introduced two manipulations. First, we virally expressed OXT1.7 in CamKII-ChR2 mice. A four-shank silicon probe (left) and tungsten wires (right) along with two optic fibers were implanted bilaterally to induce artificial ripples (Stark et al.[50]), and OXT fluorescence was measured unilaterally (Figure 7A). The optogenetically triggered ripples brought about a rapid decrease of OXT with the same latency and kinetics (ten sessions in two mice), similar to the naturally occurring ripples (Figure 7B). To test the anatomical route of the ripple-induced effect, we virally expressed the inhibitory designer receptor exclusively activated by designer drug (DREADD) in LS neurons bilaterally (AAV-DLX-hM4D(Gi)-tdTomato[49] in 3 mice. LS suppression

Please cite this article in press as: Zhang et al., Interaction of acetylcholine and oxytocin neuromodulation in the hippocampus, Neuron (2024), https://doi.org/10.1016/j.neuron.2024.02.021

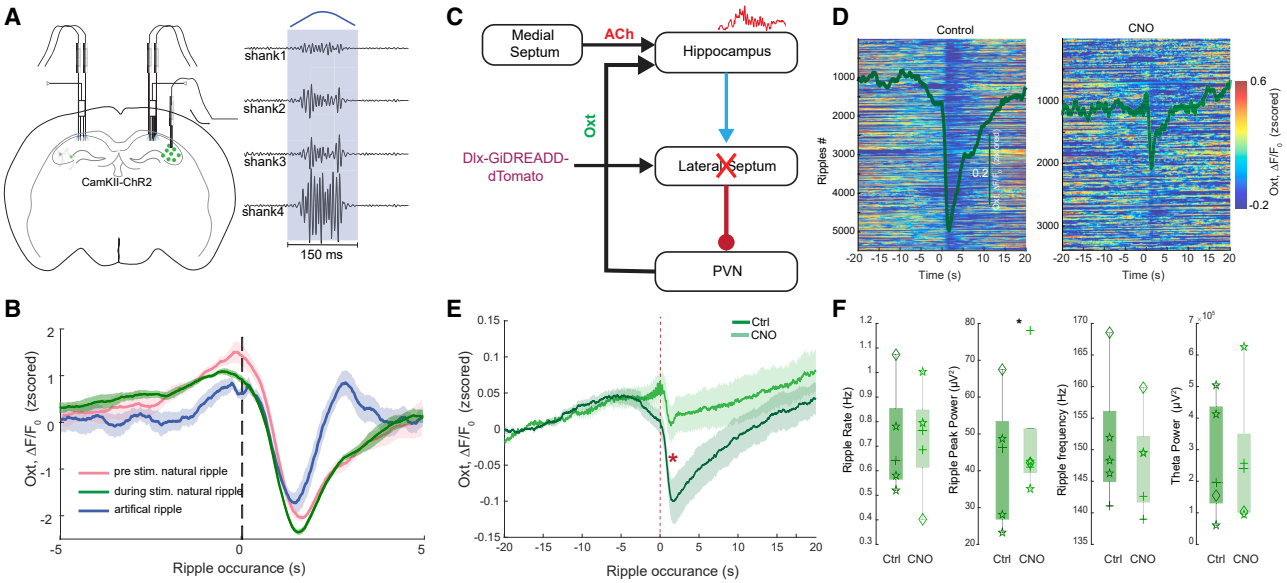

Figure 7. Hippocampal population burst-induced decrease of OXT is mediated by LS

(A) Optogenetic induction of ripples in the CA1 pyramidal layer of CamKII-ChR2 mice. Right, filtered (100–200 Hz) traces recorded from the 4 shanks of the silicon probe, blue line, Gaussian light pattern.

(B) Relationship between ripples (time 0) and OXT fluorescence (*Z* scored) in the hippocampus. Control pre-stimulation epochs (pink, spontaneous SPW-Rs, n = 5 sessions/2 mice), control spontaneous SPW-Rs interspersed with optogenetic stimulation (green), and optogenetically induced (artificial) ripples (blue). Note similar short-latency dip of OXT after both natural and induced ripples (n = 10 sessions/2 mice). p = 0.3680, one-way ANOVA.

(C) A simplified schematic representation of the hypothesized hippocampal-lateral septum (LS)-PVN path and pharmacogenetic suppression of LS activity (Tingley et al.)[49]. Blue arrow, excitation; red line/ball, inhibition. DREADD silences LS.

(D) Heatmap shows OXT fluorescence centered on SPW-Rs in saline (control) and CNO sessions in an example mouse. White line, session average.

(E) Group average of OXT fluorescence during saline sessions (n = 5 sessions in 3 mice) and CNO sessions (n = 5 sessions in 3 mice), mean ± SEM trace. ****p < 0.0001, Wilcoxon signed rank test.

(F) Comparison of SPW-R features and theta oscillation power between saline and sessions with CNO sessions. *p = 0.036; two-sample equal variance unpaired t test.

induced enhanced movement activity of the mouse; therefore, our comparisons were confined to rest periods only. During baseline recordings, SPW-Rs were followed by a rapid decrease of OXT fluorescence in the hippocampus, reaching a minimum 1.5–2 s after the SPW-R (Figure 7E, comparing with Figure 4B). During clozapin N-oxide (CNO)-induced inactivation of the LS, this relationship was significantly diminished (Figure 7E). SPW-R rate, ripple frequency, and theta band power remained unchanged after CNO injection, compared with the control (saline) session, whereas ripple peak power was moderately decreased (Figure 7F). These findings support the hypothesis that synchronous spiking events in the hippocampus can regulate OXT levels via the hippocampus-LS-hypothalamus path.

DISCUSSION

We investigated how fluctuation of ACh and OXT levels correlate with brain-state changes at long (tens of seconds) and short timescales. Although these neuromodulators worked in parallel during NREM packets, transitions from NREM to REM and NREM to WAKE were characterized by a surge of ACh but a decrease of OXT. Optogenetic and pharmacogenetic perturbation experiments demonstrated how these neuromodulators affected population activity of hippocampal circuits. Our findings demonstrate that ACh facilitates population firing rate and gamma oscillations during active waking but prevents SPW-Rs during immobility and NREM. Synchronous activity of hippocampal population consistently reduced OXT activity, mediated at least partly by the LS-hypothalamus inhibitory path. The findings demonstrate how neuromodulators can both cooperate and compete to allow target circuits to perform specific functions.

State dependence: Differential contribution of ACh and OXT to hippocampal circuit operations

One of the main postulated roles of subcortical neuromodulators is to control brain states.[51] In general, levels of neuromodulators are typically low in NREM sleep and high in the awake state.[52,53] During REM, levels of serotonin, norepinephrine, and histamine reach their lowest levels, whereas ACh levels are high.[54–56] Our findings revealed that OXT belongs to the non-ACh type of neuromodulators since OXT levels were lowest during REM.

Beyond sleep and wake state differences, previous microdialysis experiments could not examine finer relationships due to their poor temporal resolution,[57,58] whereas amperometric methods often lack specificity.[59] By contrast, GRAB sensors have both high specificity and high temporal resolution.[22,23] We observed that during NREM packets[24] (also known as ultra-slow oscillation[60–62]), lasting for 25–50 s (0.02∼0.05 Hz), ACh

Please cite this article in press as: Zhang et al., Interaction of acetylcholine and oxytocin neuromodulation in the hippocampus, Neuron (2024), https://doi.org/10.1016/j.neuron.2024.02.021

and OXT continually ramped down in parallel, coupled with gradually increasing power of delta oscillations and sleep spindles. These NREM packets are likely identical with the "cyclic alternating pattern" (CAP) of electroencephalogram (EEG) activity of NREM sleep in humans, which also terminates in microarousals.[63] The importance of these slow state fluctuations is emphasized by previous works, which showed that NREM packets support homeostatic functions and serve to normalize the firing rates of pyramidal neurons.[24,64] The NREM packets ended with REM, microarousals, or awakening,[24] heralded by a steep increase of ACh but a slow increase or decrease of OXT. Similar to ACh, Ca^{2+} imaging of norepinephrine fibers in the neocortex revealed ultraslow fluctuations during NREM and disclosed that minimum noradrenaline (NA) levels coincided with maximum spindle activity.[65,66] Identifying the specific and selective contribution of neuromodulators to these homeostatic processes will require future experiments.

The state-dependent relationship between ACh, OXT, and network events in the hippocampus was an unexpected finding. The decrease and surge of ACh produced virtually opposite changes in network activity (e.g., gamma power) during WAKE and NREM. Cholinergic activation practically abolished SPW-Rs, the most synchronous pattern in the hippocampus[30,31] during NREM, whereas during WAKE, increased spike synchrony and gamma power were linked to high ACh signals.[31] This finding implies that the effect of ACh should be evaluated against the activity level of other neurotransmitters, and their combination might determine the brain state. The relationship between ACh and OXT was not symmetric. Optogenetic activation of both cholinergic neurons and PVN OXTergic neurons suppressed SPW-Rs, but during WAKE, they showed an inverse relationship to gamma power and MUA. The most striking opposite changes of ACh and OXT signals occurred at NREM-REM transitions. Such dissociation may create metastability (i.e., a state with enhanced network switching[67]) in their common target networks, leading to state transitions. In support of this hypothesis, dopamine induces arousal in Drosophila, acting on the sleep-promoting neurons in the dorsal fan-shaped body.[68,69] Further, a transient surge of dopamine level in the basolateral amygdala of mice has been suggested to trigger NREM-REM state change,[70] although the trigger for the increased release of dopamine needs to be disclosed. ACh and dopamine (DA) can also have both positive and inverse relationships, with ACh leading the dopamine signal,[71] similar to the temporal dynamics of ACh and OXT we described here.

In summary, neuromodulators both cooperate and compete, and their competition can bring about network state transitions. Ideally, future experiments should study the covariation of multiple neuromodulators in relationship to brain states and the associated changes in circuit computation. The strong correlation between spiking features, sleep oscillations, ACh, and OXT at a slow timescale implies that neuromodulators may play a role in the homeostatic regulatory functions of sleep.

Neuromodulator relationships distinguish gamma oscillations from SPW-R

An important finding in our experiments was the neuromodulation-based separation of gamma and SPW-R oscillations. The term gamma and especially "high gamma" (50–400 Hz) are often used to refer to high-frequency LFP activity, particularly in subdural or intracranial microelectrode recordings in the human brain.[28,72,73] The frequency bands of gamma activity and ripples overlap, their durations are similar, and both are strongly correlated with neuronal spiking,[62,74–77] making their separation without multi-layer recordings and additional information difficult.[40]

Ideally, network patterns should be distinguished by their mechanisms rather than by their LFP appearance. We found that differential neuromodulation clearly distinguished gamma and ripple oscillations. High levels of both ACh and OXT reduced or prevented the occurrence of SPW-Rs. By contrast, high levels of ACh, but not that of OXT, were associated with gamma oscillations. These findings add support to previous, albeit more indirect, differentiation of these two rhythms. Gamma oscillations show behavior-dependent and layer-specific frequency bands in the hippocampus, displaying larger amplitudes in the dendritic layers than in the pyramidal layer.[35,42] By contrast, ripple power is largest in the middle of CA1 pyramidal layer and decreases rapidly toward both str. oriens and str. radiatum.[78] Power-power co-modulation of LFP signals recorded from the pyramidal layer and dendritic layers is high in the broad gamma band, whereas ripple band activity in the pyramidal layer has a negative correlation with gamma power.[33] Furthermore, gamma patterns of all frequencies are phase-locked to the theta cycles.[35,39,42,79] By contrast, SPW-Rs are absent during theta but phase-locked to sleep spindles.[80]

In addition to these behavior- and layer-specific LFP frequency band correlations, we obtained independent evidence for a switching role of neuromodulators in circuit operations. Ripple oscillations co-occurred with transient decreases of ACh reaching the highest power at the minima of ACh fluorescence, whereas gamma oscillations in the awake animal were associated with increased ACh. Gamma oscillations and SPW-Rs are controlled by different cell types.[50] For example, chandelier and O-LM interneurons are silenced specifically during SPW-Rs but fire synchronously with gamma oscillations.[36,81,82] We hypothesize that the opposite spiking relationship of these interneurons in the theta/gamma and SPW-R states and the state-dependent magnitude of population synchrony are differentially regulated by neuromodulators. In addition to our observations, this hypothesis is based on the demonstrated effects of neuromodulators on various biophysical properties of neurons, including input resistance,[83] antagonistic regulation of multiple conductance,[68,84–86] reduction of I_A,[84] and modulation of leak currents.[87] OXT not only increases activity of inhibitory hippocampal neurons and suppresses spontaneous pyramidal cell firing, but also enhances spike bursts and the fidelity of spike transmission.[88,89] In the context of our experiments, future experiments should examine whether different interneuron types have specific receptors for neuromodulators and how the combination of neuromodulators can engage or disengage them during gamma and ripple oscillations.

Long-loop hippocampal-LS path regulates OXT

An important but unsolved question is the mechanism of interactions among the various neuromodulators. Although the role of

Please cite this article in press as: Zhang et al., Interaction of acetylcholine and oxytocin neuromodulation in the hippocampus, Neuron (2024), https://doi.org/10.1016/j.neuron.2024.02.021

neuromodulators is hypothesized in brain-state regulation,[90] how evolutionarily recent structures, such as the neocortex and hippocampus, provide feedback to these neuromodulator neurons is less known. Topographic regulation of basal forebrain cholinergic neurons by the neocortex and hippocampus is well-established,[4] and recent data also support region-specific feedback regulation of dopaminergic neurons.[71] Feedback modulation of hypothalamic OXT circuits and their interactions with other neuromodulators are much less studied.[91]

Although ACh and OXT varied in parallel during NREM packets, the ACh signal preceded the OXT fluorescence by 1.5–2 s. This delay was consistently present in other brain states as well and was particularly striking after SPW-Rs and synchronous bursting of hippocampal neurons outside SPW-Rs. We replicated this temporal offset relationship by optogenetic stimulation of cholinergic neurons of the MS, which effect showed two components. The first was a large transient decrease of the OXT signal 1.5–2 s after the onset of ACh activation, followed by a smaller sustained decrease throughout the stimulation epoch. One possible mechanism for the OXT decrease is a direct suppressing effect of ACh on hypothalamic OXT-expressing neurons, although the anatomical and physiological basis of such connection needs to be established. The alternative option is a feedback loop via the hippocampus-LS-hypothalamus path.[49] Here we provide support to this indirect mechanism by demonstrating that pharmacogenetic blockade of the LS transmission strongly attenuated the impact of hippocampal neuronal activity-induced decrease of OXT activity. Note that, although our results strongly support this indirect mechanism, they do not directly test the LS-PVN portion of the circuitry. The attenuation effect was present during both SPW-Rs and MUA burst of hippocampal neurons in active waking associated with theta oscillations. This latter observation may explain why optogenetic activation of the MS leads to OXT decrease even though SPW-Rs were suppressed by cholinergic activation.[6,10,11] The tonic effect can offer a potential mechanism for the strong suppression of OXT during REM sleep, whereas the phasic effect may explain the transient dips following SPW-R of NREM. The exact hypothalamic targets of LS, such as the ventromedial or supra-optic groups,[44,92] need to be elucidated in further experiments monitoring the activity of these neuronal groups.

Potential caveats

As with all new methods, consideration should be given to potential instrumentational errors and their implication for the observations.[93] Although the GRAB-ACH3.0 sensor has been extensively tested, our experiment is the first *in vivo* application of the GRAB-OXT1.7 sensor. The *in vitro*-measured time constant of the OXT1.0 sensor is ~several times slower than that of the ACh sensor (480 vs. 150 ms at 10 μM concentration[22,23]). In our *in vivo* experiments, optogenetic stimulation of the MS yielded several times faster ACh response compared with the hypothalamic PVN stimulation-induced response, detected by the OXT1.7 sensor. However, since time constants are magnitude-dependent and we had no data about the released volume of ACh and OXT, these conclusions remain tentative. Acknowledging these caveats, our hypothesis of the cholinergic control of OXT activity likely still holds. When the fluorescent signals were aligned to the occurrence of SPW-Rs, the fastest kinetics were observed for the OXT signal by changing its magnitude 2-fold in less than 2 s, a finding that was replicated by optogenetically induced ripples. Finally, if the two neuromodulators fluctuate independently, the consistent directionality of the ACh-OXT offset cannot be simply explained by their different time constants.

The second potential caveat stems from the inevitable isolation of individual animals from their conspecifics. Isolation in our experiments was necessary because rodents often attack littermates with headgear. We acknowledge that this is a less-than-ideal situation, given the demonstration that just 1 week of social isolation may bring about changes in social preference and excitability of dopaminergic neurons.[94] Using a more compact headgear in future experiments and pairing implanted mice with littermates or allowing experimenter-supervised daily social interactions may confirm or modify the interpretation of the current results.

Conclusions

Overall, our circuit-based strategy of the relationship between network patterns and interactions between ACh and OXT can be applied to establish how interactions among different neuromodulators, converging on the same circuits, can bring about brain-state transitions. Identifying their fine timescale relationships with each other and with network events will be necessary to understand how neuromodulation supports cognition, movement control, and social interactions.

STAR★METHODS

Detailed methods are provided in the online version of this paper and include the following:

- KEY RESOURCES TABLE
- RESOURCE AVAILABILITY
  - Lead contact
  - Materials availability
  - Data and code availability
- EXPERIMENTAL MODEL AND SUBJECT DETAILS
- METHOD DETAILS
  - Surgical Procedure
  - Virus injection
  - Silicon probes and optical fiber implantation
  - ACh3.0 and OXT fluorescent signal and fiber photometry
  - Optogenetics stimulation
  - Recording and Data acquisition
  - SPW-R detection and ripple rate
  - Unit Clustering
  - LFP analysis
  - Cross-correlation analysis
  - Brain state scoring
  - Normalization of NREM packets
  - Artificial ripple generation
  - In vivo response of GRAB sensors to optogenetic stimulation
  - Pairwise correlation (synchrony)

- Detection of peaks and troughs in fiber-photometry signal
- Figure specific methods

- QUANTIFICATION AND STATISTICAL ANALYSIS

SUPPLEMENTAL INFORMATION

Supplemental information can be found online at https://doi.org/10.1016/j.neuron.2024.02.021.

ACKNOWLEDGMENTS

We thank Dayu Lin, Nicholas Tritsch, and members of their laboratories for assistance on fiber photometry and Ipshita Zutshi, Gergely Komlosi, Anna Maslarova, and Roman Huszár of the Buzsaki lab for feedback on the manuscript. In memory of Grady, Y.Z.'s cat. Supported by NIH MH122391 and U19 NS107616.

AUTHOR CONTRIBUTIONS

Y.Z. and G.B. designed the research. Y.Z., M.K., J.L., and X.G. performed the research. Y.Z. and M.K. analyzed the data. M.K. and M.V. provided technical support. Y.L. contributed new reagents. G.B., Y.Z., M.K., and R.W.T. wrote the paper.

DECLARATION OF INTERESTS

G.B. is a member of *Neuron*'s advisory board.

Received: September 11, 2023
Revised: January 17, 2024
Accepted: February 29, 2024
Published: March 26, 2024

REFERENCES

1. Ino, D., Tanaka, Y., Hibino, H., and Nishiyama, M. (2022). A fluorescent sensor for real-time measurement of extracellular oxytocin dynamics in the brain. Nat. Methods *19*, 1286–1294.
2. Jing, M., Zhang, P., Wang, G., Feng, J., Mesik, L., Zeng, J., Jiang, H., Wang, S., Looby, J.C., Guagliardo, N.A., et al. (2018). A genetically encoded fluorescent acetylcholine indicator for in vitro and in vivo studies. Nat. Biotechnol. *36*, 726–737.
3. Mesulam, M.M., Mufson, E.J., Wainer, B.H., and Levey, A.I. (1983). Central cholinergic pathways in the rat: an overview based on an alternative nomenclature (Ch1-Ch6). Neuroscience *10*, 1185–1201.
4. Záborszky, L., Gombkoto, P., Varsanyi, P., Gielow, M.R., Poe, G., Role, L.W., Ananth, M., Rajebhosale, P., Talmage, D.A., Hasselmo, M.E., et al. (2018). Specific Basal Forebrain-Cortical Cholinergic Circuits Coordinate Cognitive Operations. J. Neurosci. *38*, 9446–9458.
5. Hasselmo, M.E. (2006). The role of acetylcholine in learning and memory. Curr. Opin. Neurobiol. *16*, 710–715.
6. Zhang, Y., Cao, L., Varga, V., Jing, M., Karadas, M., Li, Y., and Buzsáki, G. (2021). Cholinergic suppression of hippocampal sharp-wave ripples impairs working memory. Proc. Natl. Acad. Sci. USA *118*, e2016432118.
7. Motley, S.E. (2018). Relationship Between Neuromodulation and Working Memory in the Prefrontal Cortex: It's Complicated. Front. Neural Circuits *12*, 31.
8. Buccafusco, J.J., Letchworth, S.R., Bencherif, M., and Lippiello, P.M. (2005). Long-lasting cognitive improvement with nicotinic receptor agonists: mechanisms of pharmacokinetic-pharmacodynamic discordance. Trends Pharmacol. Sci. *26*, 352–360.
9. Lee, M.G., Chrobak, J.J., Sik, A., Wiley, R.G., and Buzsáki, G. (1994). Hippocampal theta activity following selective lesion of the septal cholinergic system. Neuroscience *62*, 1033–1047.
10. Vandecasteele, M., Varga, V., Berényi, A., Papp, E., Barthó, P., Venance, L., Freund, T.F., and Buzsáki, G. (2014). Optogenetic activation of septal cholinergic neurons suppresses sharp wave ripples and enhances theta oscillations in the hippocampus. Proc. Natl. Acad. Sci. USA *111*, 13535–13540.
11. Ma, X., Zhang, Y., Wang, L., Li, N., Barkai, E., Zhang, X., Lin, L., and Xu, J. (2020). The Firing of Theta State-Related Septal Cholinergic Neurons Disrupt Hippocampal Ripple Oscillations via Muscarinic Receptors. J. Neurosci. *40*, 3591–3603.
12. Hampel, H., Mesulam, M.M., Cuello, A.C., Farlow, M.R., Giacobini, E., Grossberg, G.T., Khachaturian, A.S., Vergallo, A., Cavedo, E., Snyder, P.J., and Khachaturian, Z.S. (2018). The cholinergic system in the pathophysiology and treatment of Alzheimer's disease. Brain *141*, 1917–1933.
13. Froemke, R.C., and Young, L.J. (2021). Oxytocin, Neural Plasticity, and Social Behavior. Annu. Rev. Neurosci. *44*, 359–381.
14. Gimpl, G., and Fahrenholz, F. (2001). The oxytocin receptor system: structure, function, and regulation. Physiol. Rev. *81*, 629–683.
15. Leroy, F., Park, J., Asok, A., Brann, D.H., Meira, T., Boyle, L.M., Buss, E.W., Kandel, E.R., and Siegelbaum, S.A. (2018). A circuit from hippocampal CA2 to lateral septum disinhibits social aggression. Nature *564*, 213–218.
16. Lopez-Rojas, J., de Solis, C.A., Leroy, F., Kandel, E.R., and Siegelbaum, S.A. (2022). A direct lateral entorhinal cortex to hippocampal CA2 circuit conveys social information required for social memory. Neuron *110*, 1559–1572.e4.
17. Ross, H.E., and Young, L.J. (2009). Oxytocin and the neural mechanisms regulating social cognition and affiliative behavior. Front. Neuroendocrinol. *30*, 534–547.
18. Cochran, D.M., Fallon, D., Hill, M., and Frazier, J.A. (2013). The role of oxytocin in psychiatric disorders: a review of biological and therapeutic research findings. Harv. Rev. Psychiatry *21*, 219–247.
19. Guastella, A.J., Einfeld, S.L., Gray, K.M., Rinehart, N.J., Tonge, B.J., Lambert, T.J., and Hickie, I.B. (2010). Intranasal oxytocin improves emotion recognition for youth with autism spectrum disorders. Biol. Psychiatry *67*, 692–694.
20. Hitti, F.L., and Siegelbaum, S.A. (2014). The hippocampal CA2 region is essential for social memory. Nature *508*, 88–92.
21. Raymond, J.S., Rehn, S., Hoyos, C.M., and Bowen, M.T. (2021). The influence of oxytocin-based interventions on sleep-wake and sleep-related behaviour and neurobiology: A systematic review of preclinical and clinical studies. Neurosci. Biobehav. Rev. *131*, 1005–1026.
22. Jing, M., Li, Y., Zeng, J., Huang, P., Skirzewski, M., Kljakic, O., Peng, W., Qian, T., Tan, K., Zou, J., et al. (2020). An optimized acetylcholine sensor for monitoring in vivo cholinergic activity. Nat. Methods *17*, 1139–1146.
23. Qian, T., Wang, H., Wang, P., Geng, L., Mei, L., Osakada, T., Wang, L., Tang, Y., Kania, A., Grinevich, V., et al. (2023). A genetically encoded sensor measures temporal oxytocin release from different neuronal compartments. Nat. Biotechnol. *41*, 944–957.
24. Watson, B.O., Levenstein, D., Greene, J.P., Gelinas, J.N., and Buzsáki, G. (2016). Network Homeostasis and State Dynamics of Neocortical Sleep. Neuron *90*, 839–852.
25. Steriade, M., McCormick, D.A., and Sejnowski, T.J. (1993). Thalamocortical oscillations in the sleeping and aroused brain. Science *262*, 679–685. https://doi.org/10.1126/science.8235588.
26. Sullivan, D., Mizuseki, K., Sorgi, A., and Buzsaki, G. (2014). Comparison of sleep spindles and theta oscillations in the hippocampus. J Neurosci. *34*, 662–674. https://doi.org/10.1523/JNEUROSCI.0552-13.2014.
27. Buzsaki, G., and Draguhn, A. (2004). Neuronal oscillations in cortical networks. Science *304*, 1926–1929. https://doi.org/10.1126/science.1099745.
28. Canolty, R.T., Edwards, E., Dalal, S.S., Soltani, M., Nagarajan, S.S., Kirsch, H.E., Berger, M.S., Barbaro, N.M., and Knight, R.T. (2006). High

gamma power is phase-locked to theta oscillations in human neocortex. Science *313*, 1626–1628.

29. Korzeniewska, A., Franaszczuk, P.J., Crainiceanu, C.M., Kuś, R., and Crone, N.E. (2011). Dynamics of large-scale cortical interactions at high gamma frequencies during word production: event related causality (ERC) analysis of human electrocorticography (ECoG). Neuroimage *56*, 2218–2237.
30. Jones, S.R. (2016). When brain rhythms aren't 'rhythmic': implication for their mechanisms and meaning. Curr. Opin. Neurobiol. *40*, 72–80.
31. Mehta, M.R., Lee, A.K., and Wilson, M.A. (2002). Role of experience and oscillations in transforming a rate code into a temporal code. Nature *417*, 741–746.
32. Buzsáki, G. (2015). Hippocampal sharp wave-ripple: A cognitive biomarker for episodic memory and planning. Hippocampus *25*, 1073–1188.
33. Buzsáki, G., Buhl, D.L., Harris, K.D., Csicsvari, J., Czéh, B., and Morozov, A. (2003). Hippocampal network patterns of activity in the mouse. Neuroscience *116*, 201–211.
34. Buzsáki, G., Leung, L.W., and Vanderwolf, C.H. (1983). Cellular bases of hippocampal EEG in the behaving rat. Brain Res. *287*, 139–171.
35. Fernández-Ruiz, A., Oliva, A., Nagy, G.A., Maurer, A.P., Berényi, A., and Buzsáki, G. (2017). Entorhinal-CA3 Dual-Input Control of Spike Timing in the Hippocampus by Theta-Gamma Coupling. Neuron *93*, 1213–1226.e5.
36. Lasztóczi, B., and Klausberger, T. (2014). Layer-specific GABAergic control of distinct gamma oscillations in the CA1 hippocampus. Neuron *81*, 1126–1139.
37. Sullivan, D., Csicsvari, J., Mizuseki, K., Montgomery, S., Diba, K., and Buzsáki, G. (2011). Relationships between hippocampal sharp waves, ripples, and fast gamma oscillation: influence of dentate and entorhinal cortical activity. J. Neurosci. *31*, 8605–8616.
38. Scheffer-Teixeira, R., Belchior, H., Leão, R.N., Ribeiro, S., and Tort, A.B. (2013). On high-frequency field oscillations (>100 Hz) and the spectral leakage of spiking activity. J. Neurosci. *33*, 1535–1539.
39. Fernández-Ruiz, A., Oliva, A., Soula, M., Rocha-Almeida, F., Nagy, G.A., Martin-Vazquez, G., and Buzsáki, G. (2021). Gamma rhythm communication between entorhinal cortex and dentate gyrus neuronal assemblies. Science *372*, eabf3119.
40. Liu, A.A., Henin, S., Abbaspoor, S., Bragin, A., Buffalo, E.A., Farrell, J.S., Foster, D.J., Frank, L.M., Gedankien, T., Gotman, J., et al. (2022). A consensus statement on detection of hippocampal sharp wave ripples and differentiation from other fast oscillations. Nat. Commun. *13*, 6000.
41. Tort, A.B., Scheffer-Teixeira, R., Souza, B.C., Draguhn, A., and Brankačk, J. (2013). Theta-associated high-frequency oscillations (110–160Hz) in the hippocampus and neocortex. Prog. Neurobiol. *100*, 1–14.
42. Schomburg, E.W., Fernández-Ruiz, A., Mizuseki, K., Berényi, A., Anastassiou, C.A., Koch, C., and Buzsáki, G. (2014). Theta phase segregation of input-specific gamma patterns in entorhinal-hippocampal networks. Neuron *84*, 470–485.
43. Ylinen, A., Bragin, A., Nádasdy, Z., Jandó, G., Szabó, I., Sik, A., and Buzsáki, G. (1995). Sharp wave-associated high-frequency oscillation (200 Hz) in the intact hippocampus: network and intracellular mechanisms. J. Neurosci. *15*, 30–46.
44. Son, S., Manjila, S.B., Newmaster, K.T., Wu, Y.T., Vanselow, D.J., Ciarletta, M., Anthony, T.E., Cheng, K.C., and Kim, Y. (2022). Whole-Brain Wiring Diagram of Oxytocin System in Adult Mice. J. Neurosci. *42*, 5021–5033.
45. Quaresma, P.G.F., Teixeira, P.D.S., Wasinski, F., Campos, A.M.P., List, E.O., Kopchick, J.J., and Donato, J., Jr. (2020). Cholinergic neurons in the hypothalamus and dorsal motor nucleus of the vagus are directly responsive to growth hormone. Life Sci. *259*, 118229.
46. Wang, L., Meece, K., Williams, D.J., Lo, K.A., Zimmer, M., Heinrich, G., Martin Carli, J., Leduc, C.A., Sun, L., Zeltser, L.M., et al. (2015). Differentiation of hypothalamic-like neurons from human pluripotent stem cells. J. Clin. Invest. *125*, 796–808.
47. Li, X., Yu, B., Sun, Q., Zhang, Y., Ren, M., Zhang, X., Li, A., Yuan, J., Madisen, L., Luo, Q., et al. (2018). Generation of a whole-brain atlas for the cholinergic system and mesoscopic projectome analysis of basal forebrain cholinergic neurons. Proc. Natl. Acad. Sci. USA *115*, 415–420.
48. Risold, P.Y., and Swanson, L.W. (1997). Chemoarchitecture of the rat lateral septal nucleus. Brain Res. Brain Res. Rev. *24*, 91–113.
49. Tingley, D., McClain, K., Kaya, E., Carpenter, J., and Buzsáki, G. (2021). A metabolic function of the hippocampal sharp wave-ripple. Nature *597*, 82–86.
50. Stark, E., Roux, L., Eichler, R., Senzai, Y., Royer, S., and Buzsáki, G. (2014). Pyramidal cell-interneuron interactions underlie hippocampal ripple oscillations. Neuron *83*, 467–480.
51. Marder, E. (2012). Neuromodulation of neuronal circuits: back to the future. Neuron *76*, 1–11.
52. Buzsaki, G., Bickford, R.G., Ponomareff, G., Thal, L.J., Mandel, R., and Gage, F.H. (1988). Nucleus basalis and thalamic control of neocortical activity in the freely moving rat. J. Neurosci. *8*, 4007–4026.
53. Zagha, E., and McCormick, D.A. (2014). Neural control of brain state. Curr. Opin. Neurobiol. *29*, 178–186.
54. Foote, S.L., Bloom, F.E., and Aston-Jones, G. (1983). Nucleus locus ceruleus: new evidence of anatomical and physiological specificity. Physiol. Rev. *63*, 844–914.
55. Thakkar, M.M. (2011). Histamine in the regulation of wakefulness. Sleep Med. Rev. *15*, 65–74.
56. Trulson, M.E., Jacobs, B.L., and Morrison, A.R. (1981). Raphe unit activity during REM sleep in normal cats and in pontine lesioned cats displaying REM sleep without atonia. Brain Res. *226*, 75–91.
57. Hattori, T., Morris, M., Alexander, N., and Sundberg, D.K. (1990). Extracellular oxytocin in the paraventricular nucleus: hyperosmotic stimulation by in vivo microdialysis. Brain Res. *506*, 169–171.
58. Neumann, I., Ludwig, M., Engelmann, M., Pittman, Q.J., and Landgraf, R. (1993). Simultaneous microdialysis in blood and brain: oxytocin and vasopressin release in response to central and peripheral osmotic stimulation and suckling in the rat. Neuroendocrinology *58*, 637–645.
59. Estes, M.K., Freels, T.G., Prater, W.T., and Lester, D.B. (2019). Systemic oxytocin administration alters mesolimbic dopamine release in mice. Neuroscience *408*, 226–238.
60. Penttonen, M., Nurminen, N., Miettinen, R., Sirviö, J., Henze, D.A., Csicsvári, J., and Buzsáki, G. (1999). Ultra-slow oscillation (0.025 Hz) triggers hippocampal afterdischarges in Wistar rats. Neuroscience *94*, 735–743.
61. Richter, C.G., Babo-Rebelo, M., Schwartz, D., and Tallon-Baudry, C. (2017). Phase-amplitude coupling at the organism level: The amplitude of spontaneous alpha rhythm fluctuations varies with the phase of the infra-slow gastric basal rhythm. Neuroimage *146*, 951–958.
62. Watson, B.O., Ding, M., and Buzsáki, G. (2018). Temporal coupling of field potentials and action potentials in the neocortex. Eur. J. Neurosci. *48*, 2482–2497.
63. Terzano, M.G., Mancia, D., Salati, M.R., Costani, G., Decembrino, A., and Parrino, L. (1985). The cyclic alternating pattern as a physiologic component of normal NREM sleep. Sleep *8*, 137–145.
64. Miyawaki, H., Watson, B.O., and Diba, K. (2019). Neuronal firing rates diverge during REM and homogenize during non-REM. Sci. Rep. *9*, 689.
65. Kjaerby, C., Andersen, M., Hauglund, N., Untiet, V., Dall, C., Sigurdsson, B., Ding, F., Feng, J., Li, Y., Weikop, P., et al. (2022). Memory-enhancing properties of sleep depend on the oscillatory amplitude of norepinephrine. Nat. Neurosci. *25*, 1059–1070.
66. Osorio-Forero, A., Cardis, R., Vantomme, G., Guillaume-Gentil, A., Katsioudi, G., Devenoges, C., Fernandez, L.M.J., and Lüthi, A. (2021).

Noradrenergic circuit control of non-REM sleep substates. Curr. Biol. *31*, 5009–5023.e7.

67. Deco, G., Kringelbach, M.L., Jirsa, V.K., and Ritter, P. (2017). The dynamics of resting fluctuations in the brain: metastability and its dynamical cortical core. Sci. Rep. *7*, 3095.
68. Donlea, J.M., Pimentel, D., and Miesenböck, G. (2014). Neuronal Machinery of Sleep Homeostasis in Drosophila. Neuron *81*, 1442.
69. Liu, Q., Liu, S., Kodama, L., Driscoll, M.R., and Wu, M.N. (2012). Two dopaminergic neurons signal to the dorsal fan-shaped body to promote wakefulness in Drosophila. Curr. Biol. *22*, 2114–2123.
70. Hasegawa, E., Miyasaka, A., Sakurai, K., Cherasse, Y., Li, Y., and Sakurai, T. (2022). Rapid eye movement sleep is initiated by basolateral amygdala dopamine signaling in mice. Science *375*, 994–1000.
71. Krok, A.C., Maltese, M., Mistry, P., Miao, X., Li, Y., and Tritsch, N.X. (2023). Intrinsic dopamine and acetylcholine dynamics in the striatum of mice. Nature *621*, 543–549.
72. Crone, N.E., Korzeniewska, A., and Franaszczuk, P.J. (2011). Cortical gamma responses: searching high and low. Int. J. Psychophysiol. *79*, 9–15.
73. Lachaux, J.P., Axmacher, N., Mormann, F., Halgren, E., and Crone, N.E. (2012). High-frequency neural activity and human cognition: past, present and possible future of intracranial EEG research. Prog. Neurobiol. *98*, 279–301.
74. Kucewicz, M.T., Cimbalnik, J., Matsumoto, J.Y., Brinkmann, B.H., Bower, M.R., Vasoli, V., Sulc, V., Meyer, F., Marsh, W.R., Stead, S.M., and Worrell, G.A. (2014). High frequency oscillations are associated with cognitive processing in human recognition memory. Brain *137*, 2231–2244.
75. Manning, J.R., Jacobs, J., Fried, I., and Kahana, M.J. (2009). Broadband shifts in local field potential power spectra are correlated with single-neuron spiking in humans. J. Neurosci. *29*, 13613–13620.
76. Ray, S., and Maunsell, J.H. (2011). Network rhythms influence the relationship between spike-triggered local field potential and functional connectivity. J. Neurosci. *31*, 12674–12682.
77. Tong, A.P.S., Vaz, A.P., Wittig, J.H., Inati, S.K., and Zaghloul, K.A. (2021). Ripples reflect a spectrum of synchronous spiking activity in human anterior temporal lobe. eLife *10*, e68401.
78. Mizuseki, K., Diba, K., Pastalkova, E., and Buzsáki, G. (2011). Hippocampal CA1 pyramidal cells form functionally distinct sublayers. Nat. Neurosci. *14*, 1174–1181.
79. Abbaspoor, S., Hussin, A.T., and Hoffman, K.L. (2023). Theta- and gamma-band oscillatory uncoupling in the macaque hippocampus. eLife *12*, e86548.
80. Sirota, A., Csicsvari, J., Buhl, D., and Buzsáki, G. (2003). Communication between neocortex and hippocampus during sleep in rodents. Proc. Natl. Acad. Sci. USA *100*, 2065–2069.
81. Klausberger, T., Magill, P.J., Márton, L.F., Roberts, J.D., Cobden, P.M., Buzsáki, G., and Somogyi, P. (2003). Brain-state- and cell-type-specific firing of hippocampal interneurons in vivo. Nature *421*, 844–848.
82. Klausberger, T., and Somogyi, P. (2008). Neuronal diversity and temporal dynamics: the unity of hippocampal circuit operations. Science *321*, 53–57.
83. Pimentel, D., Donlea, J.M., Talbot, C.B., Song, S.M., Thurston, A.J.F., and Miesenböck, G. (2016). Operation of a homeostatic sleep switch. Nature *536*, 333–337.
84. Harris-Warrick, R.M., Coniglio, L.M., Levini, R.M., Gueron, S., and Guckenheimer, J. (1995). Dopamine modulation of two subthreshold currents produces phase shifts in activity of an identified motoneuron. J. Neurophysiol. *74*, 1404–1420.
85. Marder, E., Abbott, L.F., Turrigiano, G.G., Liu, Z., and Golowasch, J. (1996). Memory from the dynamics of intrinsic membrane currents. Proc. Natl. Acad. Sci. USA *93*, 13481–13486.
86. Nicola, S.M., Surmeier, J., and Malenka, R.C. (2000). Dopaminergic modulation of neuronal excitability in the striatum and nucleus accumbens. Annu. Rev. Neurosci. *23*, 185–215.
87. Enyedi, P., and Czirják, G. (2010). Molecular background of leak K+ currents: two-pore domain potassium channels. Physiol. Rev. *90*, 559–605.
88. Owen, S.F., Tuncdemir, S.N., Bader, P.L., Tirko, N.N., Fishell, G., and Tsien, R.W. (2013). Oxytocin enhances hippocampal spike transmission by modulating fast-spiking interneurons. Nature *500*, 458–462.
89. Tirko, N.N., Eyring, K.W., Carcea, I., Mitre, M., Chao, M.V., Froemke, R.C., and Tsien, R.W. (2018). Oxytocin Transforms Firing Mode of CA2 Hippocampal Neurons. Neuron *100*, 593–608.e3.
90. Lee, S.H., and Dan, Y. (2012). Neuromodulation of brain states. Neuron *76*, 209–222.
91. Doya, K. (2002). Metalearning and neuromodulation. Neural Netw. *15*, 495–506.
92. Osakada, T., Yan, R., Jiang, Y., Wei, D., Tabuchi, R., Dai, B., Wang, X., Zhao, G., Wang, C.X., Tsien, R.W., et al. (2022). A dedicated hypothalamic oxytocin circuit controls aversive social learning. Preprint at BioRxiv.
93. Wu, Z., Lin, D., and Li, Y. (2022). Pushing the frontiers: tools for monitoring neurotransmitters and neuromodulators. Nat. Rev. Neurosci. *23*, 257–274.
94. Musardo, S., Contestabile, A., Knoop, M., Baud, O., and Bellone, C. (2022). Oxytocin neurons mediate the effect of social isolation via the VTA circuits. eLife *11*, e73421.
95. Rossant, C., Kadir, S.N., Goodman, D.F.M., Schulman, J., Hunter, M.L.D., Saleem, A.B., Grosmark, A., Belluscio, M., Denfield, G.H., Ecker, A.S., et al. (2016). Spike sorting for large, dense electrode arrays. Nat. Neurosci. *19*, 634–641. https://doi.org/10.1038/nn.4268.
96. Vöröslakos, M., Miyawaki, H., Royer, S., Diba, K., Yoon, E., Petersen, P.C., and Buzsaki, G. (2021). 3D-printed Recoverable Microdrive and Base Plate System for Rodent Electrophysiology. Bio. Protoc. *11*, e4137. https://doi.org/10.21769/BioProtoc.4137.
97. Pachitariu M., Steinmetz N., Kadir S., Carandini M., Kenneth D, H. (2016). Kilosort: realtime spike-sorting for extracellular electrophysiology with hundreds of channels. BioRxiv. June 30, 2016. https://doi.org/10.1101/061481.
98. Petersen, P.C., Siegle, J.H., Steinmetz, N.A., Mahallati, S., and Buzsáki, G. (2021). CellExplorer: A framework for visualizing and characterizing single neurons. Neuron *109*, 3594–3608.e2.
99. Grosmark, A.D., Mizuseki, K., Pastalkova, E., Diba, K., and Buzsáki, G. (2012). REM sleep reorganizes hippocampal excitability. Neuron *75*, 1001–1007.

Please cite this article in press as: Zhang et al., Interaction of acetylcholine and oxytocin neuromodulation in the hippocampus, Neuron (2024), https://doi.org/10.1016/j.neuron.2024.02.021

STAR★METHODS

KEY RESOURCES TABLE

REAGENT or RESOURCE	SOURCE	IDENTIFIER
Bacterial and virus strains		
AAV-Ef1a-DIO-eNpHR 3.0-mCherry	UNC vector core	N/A
AAV-hDlx-GiDREADD-dTomato	Addgene	83896-AAV9
ACh3.0	W.Z Biosciences	N/A
rACh1.4	W.Z Biosciences	N/A
OXT1.7	W.Z Biosciences	N/A
AAV-EF1a-DIO-hChR2(H134R)-EYFP	UNC vector core	N/A
Chemicals, peptides, and recombinant proteins		
Dental Adhesive	Kerr Dental	Optibond
Dental Resin	Dentsply	Triad-Gel
C&B Metabond	Parkell	Cat#S380
DAPI (40,6-Diamidino-2-Phenylindole, Dihydrochloride	Thermo Fisher	D1306
Clozapine N-oxide hydrochloride	Sigma-Aldrich	SML2304
Experimental models: Organisms/strains		
Mouse: OXT-Cre	Jackson Laboratories	RRID:IMSR_JAX:024234
Mouse: ChAT-Cre	Jackson Laboratories	RRID:IMSR_JAX:006410
Mouse: Ai32	Jackson Laboratories	RRID:IMSR_JAX:012569
Mouse: C57BL/6J	Jackson Laboratories	RRID: IMSR_JAX: 000664
Software and algorithms		
KiloSort (template based spike sorting MATLAB software	Pachitariu M & Cortex-lab	https://github.com/cortex-lab/KiloSort
KilosortWrapper	Peter C. Petersen & Brendon Watson	https://github.com/petersenpeter/KilosortWrapper
Phy (Python GUI for manual spike curation)	Cyrille Rossant, Ken Harris et al.[95]	https://github.com/cortex-lab/phy
Phy plugins	Peter C. Petersen	https://github.com/petersenpeter/phy-plugins
MATLAB	MathWorks	https://www.mathworks.com/
Buzcode (MATLAB analysis tools)	Buzsaki Lab	https://github.com/buzsakilab/buzcode
FMA Toolbox (MATLAB toolbox for Freely Moving Animal (FMA))	Michael Zugaro	https://fmatoolbox.sourceforge.net/
Custom MATLAB scripts	This paper	will be available in Github
Sleep State Score Curation	Zeke Barger	https://github.com/zekebarger/AccuSleep
Control Softwares	This paper	will be available in Github
Other		
RHD2000 USB Interface Board	Intan Technologies	C3100
64 channel digital amplifier	Intan Technologies	C3314
PulsePal v2	Samworks	N/A
3D printed microdrives	Mihály Vöröslakos & Gyorgy Buzsaki	Voroslakos et al.[96]
Silicon probes	Neuronexus, Diagnostic Biochips	Poly3, 128 2 shank
Data adquisition interface Power3A	Cambridge ElectronicDesign Limited (CED)	Power1401-3A
6 port Fluorescence Mini Cube	Doric	FMC6_IE(400-410)_E1(460-490)_F1(500-540)_E2(555-570)_F2(580-680)_S

(*Continued on next page*)

Please cite this article in press as: Zhang et al., Interaction of acetylcholine and oxytocin neuromodulation in the hippocampus, Neuron (2024), https://doi.org/10.1016/j.neuron.2024.02.021

Continued

REAGENT or RESOURCE	SOURCE	IDENTIFIER
Fluorescence Detector	Newport	2151
Blue and Yellow LEDs	Thorlabs	M470F3, M565F3
Optogenetic Blue Laser	CNI Laser	MBL473
AOM controller	AA Opto-Electronic	MTS110-A3-VIS
Optic Fiber	Thorlabs	FP200URT, FP400URT
Instrumentation Amplifier	Brown Precision	Model 440
Signal Generators	Rigol and Keithley	DG4062, 3390
Fiber Coupler	Thorlabs	PAF-X-11-PC-A
OptiTrack 5-camera system	Natural Point Corp.	Flex 3

RESOURCE AVAILABILITY

Lead contact

Further information and requests for resources should be directed to the lead contact, György Buzsáki (gyorgy.buzsaki@nyumc.org).

Materials availability

This study did not generate new unique reagents.

Data and code availability

All data and code referenced in each subfigure is available at (https://buzsakilab.nyumc.org/datasets/ZhangY/Neuon_2024/). All raw electrophysiological and sensor imaging data will be provided upon reasonable request. Any additional information required to re-analyze the data reported in this paper is available from the lead contact upon request.

EXPERIMENTAL MODEL AND SUBJECT DETAILS

All experiments were approved by the Institutional Animal Care and Use Committee at New York University Langone Medical Center. Mice were housed in groups before surgery and singly after surgery under a reverse 12-hour light-dark cycle (dark from 6 a.m. to 6 p.m.) with ad libitum access to food and water. Experiments were carried out using both male and female mice at 3-6 months of age. OXT-Cre and ChAT-Cre transgenic mouse lines were used or crossed with Ai32 transgenic mice to generate OXT-ChR2 and ChAT-ChR2 mouse models, respectively. The OXT-Cre, ChAT-Cre, and Ai32 mice were obtained from The Jackson Laboratory and allowed to acclimate for several weeks prior to their utilization in experimental procedures.

METHOD DETAILS

Surgical Procedure

All experiments were approved by the Institutional Animal Care and Use Committee at New York University Langone Medical Center (NYULMC). General anesthesia was induced with isoflurane inhalation. For survival surgery (injection of virus, or implantation of probes and optical fibers), anesthesia was maintained by isoflurane through a mask mounted on the stereotaxic apparatus. Body temperature was kept constant with a heating pad (37 °C).

Virus injection

Under aseptic conditions, the skull was exposed using local anesthesia comprising 4% lidocaine. Subsequently, holes were drilled above specific brain regions, namely the medial septum (pAAV-Ef1a-DIO-eNpHR 3.0-mCherry), lateral septum (AAV-hDlx-GiDREADD-dTomato), hippocampus CA1 (ACh3.0), and CA2/CA3a (rACh1.4 and OXT1.7). The coordinates for targeting these regions were as follows: medial septum (anteroposterior [AP] +0.7 to +0.9 mm, midline insertion at 0° angle), lateral septum (AP +0.49 mm, mediolateral [ML] ±0.5 mm), and hippocampus (AP -2 mm, ML +1.5mm (CA1) or +2.3 mm (CA2/CA3a).

For viral injections, a glass pipette with a tip size of 30 to 50 μm, connected to a Nanoject II/Nanoliter 2000 microinjector (Drummond Scientific Co. or WPI Inc.), was employed. Within the medial septum, 0.05 to 0.07 μL of virus solution was injected at three different depths between 3.2 and 4.0 mm (midline, 0° angle). For the lateral septum, 0.2 μL of virus solution was injected at depths of 3.3 and 3.8 mm on both sides. In the hippocampus, 0.1 μL of virus solution was injected at depths of 1.25 and 1.75 mm in CA1, 1.7 and 2.3 mm in CA2/CA3a. The injection duration was 15 minutes.

After the completion of each injection, the pipette was slowly retracted in 0.1 mm and then 0.5 mm steps, with a 10-minute interval between each retraction. Finally, the scalp was sutured to close the surgical site.

Please cite this article in press as: Zhang et al., Interaction of acetylcholine and oxytocin neuromodulation in the hippocampus, Neuron (2024), https://doi.org/10.1016/j.neuron.2024.02.021

Silicon probes and optical fiber implantation

In the medial septum (MS), a lambda fiber with a diameter of 200 μm and an active length of 1.5 mm was surgically implanted at a depth of 4 mm, at a 10° angle (Plexon). For targeting the paraventricular hypothalamic nucleus (PVN), 200 μm diameter optical fibers were bilaterally implanted at a depth of 4.5 mm, at 5°. Prior to the surgical procedure, the outer layer of the optic fiber was removed, and 1.25 mm ceramic ferrules, extracted from LC connectors (Thorlabs), were attached for optimal connectivity. To facilitate brain insertion and enhance light scattering, the fiber tip was sharpened through a 30-second etching process in hydrofluoric acid (Sigma).

To enable fiber photometry measurements, an optic fiber with a diameter of 200 μm (Thorlabs FP200URT, NA=0.5) or 400 μm (Thorlabs FP400URT, NA=0.5) was surgically implanted into the hippocampus at the coordinates of AP -2 mm, ML 1.6 mm, and DV 1.5 mm. This optic fiber served to capture the emitted fluorescent signal from the sensor, facilitating the collection of data for subsequent fiber photometry analysis.

Silicon probes (NeuroNexus, 64 sites, 4 shanks. Diagnostic biochips, 4 or 2 shanks) were carefully inserted into the hippocampal CA1 or CA2 regions at depths ranging from 1 to 2.5 mm. The silicon probes were securely affixed to a microdrive and gradually lowered into the CA1 pyramidal layer at a depth of 0.7 mm. Following a 72-hour post-surgical recovery period, the probes were incrementally lowered by 1/8th of a cycle of the screw at a time, with a subsequent waiting period of 2 hours before commencing recording at each depth. The lowering process continued until the hippocampal area was reached, identified by the presence of distinctive ripples and robust neuronal spiking activity. The depth adjustment was then halted upon reaching the target hippocampal region.

ACh3.0 and OXT fluorescent signal and fiber photometry

For single-sensor recordings, we employed a 400 Hz square-wave train to drive both a light-emitting diode (LED) at 470 nm (LED-driver, model LEDD1B) and a fiber-coupled LED (model M470F3) from Thorlabs. These light sources were controlled by a Rigol DG4062 Arbitrary Waveform Generator. The optical excitation was directed towards the ACh3.0 sensor. To measure the light power, a Thorlabs PM100D power meter was utilized at the tip of a mono fiber optic patch cord (model FC-MF1.25), resulting in a recorded power range of 30 to 100 μW in an air environment. The actual power reaching the brain was maintained at 80% to 95% of the input power. For the excitation process, a frequency of 400 Hz was selected, along with a duty cycle of 60%. The light excitation and subsequent fluorescence detection were facilitated through a Mini cube featuring three ports (Doric FMC6_E1(465-480)_F1(500-540)_E2(555-570)_F2(580-680)_S). The emission light emitted by the ACh3.0 signal was transmitted back through the same optical fiber and subjected to bandpass filtration (500 to 550 nm) within the Minicube. The fluorescence signal was then captured by a Femtowatt Silicon Photoreceiver (manufactured by Newport, model 2151). The detected signal passed through a lowpass filter (Model 440 instrumentation Amplifier) at 20 Hz and recorded using a real-time processor (CED power 1401). The ACh3.0 fluorescence response was calculated by the equation $\Delta F//F_0 = (F-F_0)/F_0$, in which the F_0 is the baseline signal detected by a fifth-order polynomial fitting.

To excite the OXT1.7 and rACh1.4 sensors simultaneously, we used fiber-coupled LEDs at 470 nm (Thorlabs M470F3) and 561 nm (Thorlabs M565F3), respectively. Excitation light was passed through a fiber optic patch cord (Doric 400 μm 0.48 NA) to the fluorescence mini-cube (Doric FMC6_E1(465-480)_F1(500-540)_E2(555-570)_F2(580-680)_S) and connected to the chronic optic fiber implant in the mouse via a fiber optic patch cord (Doric 400 μm 0.48 NA). The emission light of OXT1.7 and rACh1.4 in the dorsal hippocampus was collected through the same patch cord and fluorescence mini-cube, which was connected to two Femtowatt Silicon Photoreceivers (Newport, 2151); one for green emitted light, and another for the red emitted light. Excitation light was delivered in frequency-modulated (FM) mode by two Waveform Generators. Two sinusoids generated using the signal generator (311Hz, Rigol DG4062 Arbitrary Waveform Generator; 219Hz, Keithley 3390 50MHz Arbitrary Waveform Generator) were used to drive the fiber-coupled LED. The 470 nm and 561 nm LEDs were modulated at 311 Hz (OXT1.7) and 219 Hz (rACh1.4), respectively. Light power (30-100 μW) was set by adjusting the amplitude and offset parameters of the sinusoidal control voltage by monitoring a photodiode power controller (S130C, Thorlabs) coupled with a power meter (PM100D; Thorlabs).

Photometry signals read out by the photoreceiver were digitized using a real time processor (CED power 1401) at 20 kHz. We used a conventional quadrature demodulation technique, involving the phase-shifting of the reference signal by 90 degrees before multiplication with the reference excitation sinusoid. The resultant signal was subsequently subjected to low-pass filtering at 20 Hz using a 4th order Butterworth filter. The demodulated signals were calculated by taking the square root of the sum of the squares of the in-phase and quadrature components. Then, the signal was down sampled to 100 Hz and baseline was adjusted as described. (details were described in Figure S2.)

Optogenetics stimulation

The brain-implanted optic fiber was illuminated using a diode-pumped solid-state laser (DPSS) emitting light at a wavelength of 473 nm for activation or fiber coupled 589 nm (CNI Laser MGL-589) for inhibition. In dual color acquisition, photostimulation using a 473 nm diode-pumped solid-state laser (CNI Laser MBL473, 200 mW) was used for photostimulation. Its timing and power were controlled by an acousto-optic modulator (AA Opto-Electronic, MTS110-A3-VIS). The output is coupled to fiber via a coupler (PAF-X-11-PC-A, Thorlabs). Light intensity was controlled using analog modulation of custom scripts driving PulsePal (Sanders and Kepecs, 2014) to generate sinusoidal patterns or pulse patterns, and the voltage input was adjusted such that it could deliver between 5 mW and 18 mW. For optogenetic activation, a frequency of 20 Hz with a 30% duty cycle was employed, while a constant light stimulus of 5 seconds was utilized for inhibition. To achieve optimal stimulation of the target regions, the maximum light

intensity (defined as the crest of the sine wave or plateau pulse amplitude) was fine-tuned using a photodiode power controller (S130C, Thorlabs) coupled with a power meter (PM100D; Thorlabs). The measurements of patch-cord-to-fiber coupling, performed prior to fiber implantation, were taken into consideration to ensure a maximum power of 5 to 10 mW at the fiber tip within the brain.

Recording and Data acquisition

Recordings were conducted using the Intan RHD2000 interface board, sampled at 20 kHz. Amplification and digitization were done on the head stage. For chronic recording, animals were recorded in their home cage during sleep, alert immobility, or actively awake (grooming, sniffing, etc.) and/or during the exploration of a different environment (50 × 50-cm open field arena or 1 meter linear track. The position of the animal was tracked with an OptiTrack 5-camera system (Natural Point Corp.). Calibration across cameras allowed for a three-dimensional reconstruction of the animal's head position and orientation. A rigid body was created by mounting 6 reflective markers to a small 3D-printed holder, attached to the animal's head-cap and tracked simultaneously by 6 infrared cameras (OptiTrack, Flex 3 cameras) at 100Hz (Petersen and Buzsaki, 2020). The TTL signal generated by Optitrack was used for synchronizing the Ephys and fiber photometry signals.

SPW-R detection and ripple rate

The LFP from a selected channel (largest ripple power) was 140-250Hz bandpass-filtered by a 4th order Butterworth filter, and then the Hilbert transform was applied to filtered LFP to get ripple band amplitude. Candidate events were detected by choosing the periods that the ripple band amplitude is 2 standard deviations (SD) above the mean, peak amplitudes >5 SD, and duration between 30-200ms. After that, SPW-Rs were manually selected from candidate events by looking at the raw LFPs from neighboring channels. Ripple rate was determined using 0.5 s (Figure 3B) or 3 s (Figure 3C) time window and smoothed by a moving average of 1.5 or 9 s.

Unit Clustering

Spike extraction and classification were conducted using Kilosort (Pachitariu et al.[97]) with a specialized pipeline called KilosortWrapper (https://github.com/brendonw1/KilosortWrapper). The automated sorting process was subsequently complemented by manual curation of the waveform clusters. This manual refinement was in Phy (https://github.com/cortex-lab/phy), along with custom plugins specifically designed for Phy (https://github.com/petersenpeter/phy1-plugins). Distinct units were categorized into potential pyramidal cells and narrow waveform interneurons based on various criteria, including their autocorrelograms, waveform properties, and firing rates. This classification process was executed in CellExplorer.[98]

LFP analysis

The 20kHz recorded raw data was low-pass filtered by a sinc filter with a 450 Hz cut-off band, and then downsampled to 1250Hz to get the local field potential (LFP). The power spectrogram was calculated using short-time Fourier transform. For delta, theta, slow gamma, fast gamma, ripple power analysis, the LFP was bandpass-filtered by 0.5-4 Hz, 5-10 Hz, 30-80 Hz, 80-120 Hz, 140-250 Hz, respectively. The band powers were calculated using Chronux multi-taper spectrum methods and smoothed with 1-s moving mean window. Theta score is defined as the ratio of power in theta band and delta band). The correlation between LFP power and ACh3.0 signal is measured as Pearson correlation coefficient. The cross-correlations between ACh3.0 signal and gamma power (slow and fast, separately) or ripple power were generated from normalized data of each session.

Cross-correlation analysis

The cross correlation of variable x[n] and a lagged version of y[n] by k units is calculated as

$$R_{xy}[k] = \frac{R_{xy}[k]}{\sqrt[2]{R_{xx}[k]R_{yy}[k]}}$$

where $R_{xy}[k] = E\{x[n]y[n-k]\} = \sum_{-\infty}^{\infty} x[n]y[n-k]$

This calculation allows to quantify the similarity or relationship between these x[n] and y[n] at a specific time lag k.

Brain state scoring

Sleep states were identified through an automated scoring algorithm described in previous studies.[24,98] This method involves the extraction of three signals from the recording: broadband LFP, narrowband theta frequency LFP, and EMG. After the automated scoring, all detected states were reviewed manually by experimenters. Minor adjustments were made based on the signals from the EMG and accelerometer.

Normalization of NREM packets

We have detected every microarousals in each NREM episode, as shown in Figure 2A. Each NREM packet is defined as the interval between two consecutive microarousals. The duration of each NREM packet is normalized between 0 (start) and 1 (end).

Please cite this article in press as: Zhang et al., Interaction of acetylcholine and oxytocin neuromodulation in the hippocampus, Neuron (2024), https://doi.org/10.1016/j.neuron.2024.02.021

Artificial ripple generation

In experiments involving optogenetic induction of hippocampal ripples, mice expressing CamKII-ChR2 (n = 2) were used. For each hemisphere, a microdrive was assembled with either silicon probes or tungsten wires offset by 400-800 μm along the medial-lateral axis. The microdrive was advanced until a CA1 ripple pattern was observed. For optogenetic stimulation, two 200-μm optic fibers were attached to this microdrive, positioning the fiber tips 200–400 μm above the most dorsal recording site. The fiber photometry signal was recorded in one hemisphere where a GRAB sensor had been injected for 3 weeks. The light power at the fiber tip was adjusted to be ~200 μW. A 150 ms light pulse was applied at a mean rate of 0.4 Hz to generate artificial ripples. To reduce light artifacts, the shape of the pulse was set to be half sinusoidal.

In vivo response of GRAB sensors to optogenetic stimulation

Since OXT1.7 is an intermediate version of our oxytocin sensor, we have not characterized its kinetics in HEK cells or in vitro. To assess their hippocampal response kinetics to optogenetic stimulation of the medial septum or PVN, we determined the in vivo kinetics based on optogenetically evoked responses in Figure 5. The response and recovery time constants were calculated using the following equations, fitting to the response and recovery phases separately:

$$f_{response}(t) = a_1\left(1 - e^{-\frac{t}{T_{response}}}\right) + c_1, f_{recovery}(t) = a_2 e^{-(t-t_{off})/T_{recovery}} + c_2$$

Pairwise correlation (synchrony)

Synchrony was quantified by computing the mean pairwise correlations among firing rates of pyramidal cell-pyramidal cell pairs, interneuron-interneuron pairs, and pyramidal-interneuron pairs. The firing rates were binned in non-overlapping 100 ms intervals, as described here.[99]

Detection of peaks and troughs in fiber-photometry signal

We used the MATLAB built-in function (findpeaks) to identify peaks and troughs within the dataset. This function facilitates the identification of local maxima through a straightforward comparison of neighboring values. To refine the selection of peaks, we employed specific options within the function to impose conditions on the properties of the detected peaks. Notably, a minimum peak amplitude criterion of 0.05 was selected, ensuring that only prominent peaks were considered. Additionally, a constraint was set on the minimum distance between adjacent peaks, requiring a separation of at least 0.2 seconds. By carefully configuring these parameters, our analysis targeted peaks with significant amplitude and temporal distinctiveness. For detection of troughs, we multiply the photometry signal by –1, and then use the same procedure as above.

Figure specific methods

Figure 1E: To optimize visual clarity, the scatter plot was downsampled by factors of 50 for acetylcholine (ACh) data and 30 for oxytocin (OXT) data.

Figure 1F: ACh data was extracted from the behavioral data. The initial 200 seconds of ACh data were excluded to exclude the potential influence of transient effects or artifacts. z-scored theta scores exceeding 3 were omitted.

Figure 2A: Shading interpolation was used for the smoothing of heatmaps to enhance the salience of underlying patterns.

Figure 4: Standardization of ACh and OXT signals across each session and animal was achieved through z-scoring and then ripple event-triggered averages were calculated for distinct ripple rates to elucidate potential relationships between these neuromodulators and ripple events.

Figure 5: The firing rate traces has been smoothed using a Gaussian kernel

Figure 7B: To facilitate visual comparison of temporal dynamics in OXT signals, individual traces were z-scored within a time window of -5 to 5 seconds relative to artificial ripple events.

Figure 7D: A moving average of 0.15 seconds was applied to the time axis of the heatmap.

QUANTIFICATION AND STATISTICAL ANALYSIS

Quantification and statistical analyses were conducted using MATLAB or GraphPad Prism 10. Comprehensive details regarding the analysis for each figure have been elucidated in the text or figure legend.